Global and local geometrical imperfections of pultruded GFRP profiles based on a modal approach

João Alfredo de Lazzari [a],[*], Luís Lages Martins [b], Álvaro Silva Ribeiro [b], Alexandre Pinheiro [b], João Ramôa Correia [a], Nuno Silvestre [c]

[a] CERIS, Instituto Superior Técnico, Universidade de Lisboa, Av. Rovisco Pais 1, 1049–001 Lisboa, Portugal
[b] LNEC, National Laboratory for Civil Engineering, Scientific Instrumentation Centre, Av. do Brasil, 101, 1700–066 Lisboa, Portugal
[c] IDMEC, Instituto Superior Técnico, Universidade de Lisboa, Av. Rovisco Pais 1, 1049–001 Lisboa, Portugal,

ARTICLE INFO

ABSTRACT

The ultimate capacity of pultruded glass fibre reinforced polymer (pGFRP) profiles depends significantly on geometrical imperfections (GIs), given their sensitivity to buckling phenomena arising from both thin walls and low elastic moduli. However, GIs are not yet comprehensively addressed in design guidance. This paper proposes a new approach to characterize the initial GIs of pGFRP profiles based on a modal approach. Given the lack of comprehensive knowledge in this area, this study presents a highly accurate and robust methodology to measure GIs and dimensional deviations (DDs) in pGFRP profiles using a 3D contact coordinate measurement machine (CMM). The modal approach encompasses the measurement of dimensional parameters and a point cloud transformation that enables the assessment of GIs associated with pure buckling modes of pGFRP profiles. This procedure allows the quantification of three types of global GIs associated to (i) minor-axis (weak axis), (ii) major-axis (strong axis) bending, and (iii) twist. Additionally, the procedure also includes the assessment of local GIs, considering the wall (plate-like) imperfections. The separation of GIs into these four types (shape and amplitude) is of major relevance as its paves the way to the development of analytical design formulas for the strength prediction of pGFRP members. The approach described in this paper also serves two important purposes: (i) the statistical analysis of DDs and GIs of pGFRP members, and (ii) the identification of distinct shapes and amplitudes of GIs that form the basis for reliable design considerations of pGFRP members.

1. Introduction

1.1. Background

In recent decades, there has been a rise in the costs associated with repairing and maintaining civil engineering structures. This trend has led to an increased demand for constructions that are lighter, faster, and offer improved durability with lower maintenance requirements. To meet these demands, pultruded glass-fibre reinforced polymer (pGFRP) profiles have emerged as a competitive solution due to their high strength-to-weight ratio and corrosion resistance [1,2]. However, pGFRP profiles often exhibit high deformability and susceptibility to buckling due to their relatively low elastic moduli and thin-walled cross-sections. Buckling phenomena frequently govern the strength

---

and design of pGFRP profiles. In particular, initial geometrical imperfections (GIs)[1] play a crucial role in the post-buckling behaviour of pGFRP profiles [3].

Most existing techniques for measuring GIs in prismatic structural members have been primarily conducted on thin-walled steel structures [4–20]. However, it is important to note that pGFRP members share similar shapes with the first generation of steel cross-sections and exhibit high slenderness characteristics with respect to both local and global buckling phenomena, primarily due to their relatively low elastic moduli. Consequently, these pultruded elements can be classified as thin-walled cross-sections [2].

A significant amount of research has been dedicated to determine the GIs of thin-walled steel members used in civil engineering structures [21]. Given the substantial geometric similarities between pGFRP profile shapes and traditional steel profiles, existing methodologies for measuring GIs in steel structures are a valuable starting point for determining GIs in pGFRP profiles. In this context, existing techniques for measuring GIs in thin-walled prismatic steel structures can be broadly categorized into two groups: (i) contact measurements [4–11] and (ii) non-contact measurements [12–20]. Contact measurement techniques utilize electromechanical devices, like dial gauges, displacement transducers and linear variable differential transformers (LVDTs), whereas non-contact measurement techniques employ optical techniques, such as laser scanning (LS). LS techniques can be further classified into various types, including arm type [13,15], handheld type [14,16,19,20], structured light type [17], terrestrial type [18,22] and custom platforms [12].

The evaluation of GIs has been a major research topic in thin-walled steel structures [4–20]. In terms of contact measurement methodologies, Rasmussen & Hancock [4] conducted measurements at six different locations along a cold-formed steel (CFS) channel section to analyse its buckling behaviour. Young & Rasmussen [5] used transducers attached to a movable frame to measure GIs in CFS lipped channel columns. Other contact methods have been employed to characterize the GIs of CFS profiles. These include the use of a direct current differential transformer (DCDT) in conjunction with a milling machine [6], a custom-built setup featuring a digital dial gauge and a portable rig [7,8], and a moving device equipped with LVDTs that continuously travels along the column's length, monitored by a potentiometer displacement transducer [9–11]. Recently, building upon this moving device contact measurement methodology, Salles *et al.* [23,24] developed an analytical modal decomposition procedure, which enabled a direct estimation of the shape and amplitude of the most common GIs associated with buckling modes observed in experimental tests of CFS lipped channel sections [10].

Non-contact measurement techniques have also been employed using LS-based platforms to assess the GIs of metallic structures. Zhao *et al.* [12] developed a platform consisting of a rotary ring attached to a linear motion system with a line LS to measure the full-field geometry of CFS members. Selvaraj and Madhavan [13] used a two-folded arm LS method to measure GIs of 188 CFS channel sections. Feng *et al.* [14] devised a methodology based on handheld 3D LS to assess GIs, thus enabling the study of imperfection reduction in steel I-sections through pre-stressed carbon fibre-reinforced polymer strips. Gardner *et al.* [15] also used a portable 3D measuring arm LS to assess the surface geometry of circular hollow section stub columns manufactured by additive manufacturing. Zhang *et al.* [16] employed a handheld 3D LS method to evaluate GIs in steel box-T section columns. Erkal and Cagrici [17] employed a mobile 3D structured light scanner to assess GIs in CFS members, while Nascimento *et al.* [18] examined the web out-of-plane GIs of steel plate girders with intermediate transverse stiffeners using terrestrial LS. Xu *et al.* [19] utilized a handheld LS technique to measure

the geometric imperfections of 71 specimens comprising four common types of steel tubes, and Xu *et al.* [20] proposed a handheld 3D LS for obtaining full-field GIs in steel members.

Being a traditional construction material, CFS is now well integrated into design standards [25–28] and the GIs of CFS structural members are nowadays well characterized and fairly understood. The same does not happen in case of pGFRP profiles. To the best of the authors' knowledge, comprehensive studies on the characterization of GIs in pGFRP profiles are lacking in the existing literature. Thus, it is necessary to obtain a more in-depth knowledge on this topic, including the characterization of GIs in pGFRP members and the development and assessment of methodologies for such characterization.

1.2. Overview of the current knowledge of GIs in pGFRP members

The earliest work on GI measurement in pGFRP columns was published by Yoon [29] in 1993. Yoon measured the out-of-straightness of twenty pGFRP columns using a dial gauge. The columns were positioned on a level table, and their out-of-straightness was measured in the flanges and taken as the differential depth between the member and the table plane. The measured out-of-straightness values ranged from $L/896$ to $L/273$ (with an average value of $L/392$ – hereafter, L is considered the member length), which are lower than the current ASTM D3917 [30] standard tolerance ($L/240$). Subsequently, Brooks & Turvey [31] measured the out-of-straightness of an I-beam at three different positions (top flange, bottom flange, and web centreline), but their methodology was not clearly described. In 1997, Zureick & Scott [32] and Zureick & Steffen [33] conducted GI measurements on pGFRP profiles with wide-flange, box, and angle cross-sections. They used a lathe table with a moving dial gauge along the pGFRP specimen and found that the measurements were within the deviation tolerances specified in ASTM D3917 [30]. Lane and Mottram [34] employed a surveying theodolite to measure the maximum minor-axis out-of-straightness of wide-flange cross-sections and concluded that the influence of GIs on the failure load was negligible. In a subsequent study, Mottram *et al.* [35] characterized the cross-section sizes and measured the minor-axis out-of-straightness of pGFRP wide-flange columns at five different cross-sections along the axis. They obtained a maximum value of $L/4800$ and concluded that the limits specified in ASTM D3917 [30] are excessive, emphasizing the need to reduce the allowance for out-of-straightness imperfections.

In the past decade, Nguyen *et al.* [36,37] conducted measurements of the minor-axis GI of C and I-sections. The setup involved a displacement transducer mounted on a movable track runner, which measured the web out-of-plane displacements at mid-depth every 100 mm along the length of the profile. Based on measurements performed on 16 beam elements with lengths ranging from 1828 mm to 3454 mm, the authors obtained GIs ranging from L/9048 to L/421 for C-sections and from L/2436 to L/874 for I-sections. They concluded that the lateral-torsional behaviour of pGFRP beams is highly influenced by GIs and that the current out-of-straightness limit $L/240$, specified in ASTM D3917–15 [30], is excessively high and inappropriate.

Aiming to establish a GI factor for predicting the strength of square hollow section (SHS) pGFRP columns, Cardoso *et al.* [38] employed the Southwell plot analysis [39] to determine their GIs. Monteiro [40] utilized a more precise method for GI measurement of pGFRP angle sections, employing an arm type 3D coordinate measuring machine (CMM) with an accuracy of 0.1 mm. The author measured the out-of-plane displacements at five different cross-sections along the profile axis, with six points per cross-section (three points in each flange). The obtained out-of-straightness values were relatively small compared to the profile length, ranging from $L/4894$ to $L/2080$.

Since the turn of the XXI century, computational analyses using finite element (FE) models have been complementing with great accuracy the experimental data obtained from tests. Therefore, it is no surprise to observe the current frequent use of FE analysis to evaluate the strength

---

[1] Hereafter, the "initial GIs" are simply designates as "GIs", because they always exist prior to the application of loads, i.e., in the initial state.

of pGFRP members. Like in case of CFS members, an accurate simulation of pGFRP columns and beams requires the consideration of realistic GIs. However, due to limited available GI data, various assumptions have been made in previous numerical studies. Turvey and Zhang [41] incorporated GIs in an FE model of a column by assuming they have the shape of the first critical buckling mode with an amplitude of 0.002 mm. Laudiero *et al.* [42,43] performed computational simulations and found out that the prescribed limits of GI amplitudes provided by manufacturers [44,45] and standards [30,46], often very high, resulted in excessively conservative strength estimates of pGFRP members. Conversely, the adoption of lower amplitudes reported in the literature (based on experimentally measured GIs by Nguyen [37]) led to less conservative strength predictions and more realistic failure mechanisms of pGFRP members. Ascione *et al.* [47] performed a GI sensitivity analysis using FE simulations and considered three different I-section geometries, three maximum amplitudes ($L/1000$, $L/500$ and $L/250$) and quadratic out-of-straightness GI shape, and they concluded that the GI has a significant impact on the nonlinear behaviour of slender beams. Nunes *et al.* [48] conducted a computational study on the strength of hybrid pFRP beams, which incorporated the Hashin damage criterion, progressive material failure, second-order effects induced by compression, and GIs determined by the Southwell-plot method [39]. They also explored various GI amplitudes for columns with different lengths [49], and accounted for local, global, and local-global interactive buckling failure modes. Chawla and Sing [50] conducted nonlinear analyses of pGFRP beams, having a GI with the shape of the first (critical) buckling mode and an amplitude of 0.1% of the cross-section height. In a recent computational study, Nguyen *et al.* [51] examined the combined effect of GIs on the strength of pGFRP beams. The authors incorporated GIs in beams spanning from 1900 mm to 4100 mm by assuming the shape of a sinusoidal wave with maximum amplitude obtained from experimental tests [37]. Anbarasu *et al.* [52] considered the shape of GIs in a design proposal to estimate the axial capacity of pGFRP channel columns. They assumed the GI with the shape of the first (critical) buckling mode and adopted two different amplitudes: (i) 10% of the thickness for the local buckling mode GI, previously proposed by Czapski and Kubiak [53], and (ii) $L/500$ for the global buckling mode GI, following the guidelines provided in the Fiberline design manual [54].

The available standards for the execution of composite structures and the production tolerances of pGFRP members impose upper bounds to GIs, as well as dimensional deviations (DDs), as shown in Fig. 1. The European standard EN 13706–2 [46] and the Chinese standard GB/T 31539 [55] share similar limits on DDs, whereas the North American standard ASTM D3917–15a [30] imposes less stringent limits, allowing for larger DD tolerances (Fig. 1a). Regarding the out-of-straightness GIs for open-sections, ASTM D3917–15a is a bit more strict than EN 13706–2 for the following member length ranges: (i) $L > 2085$ mm (B or $H < 50$ mm), (ii) $L > 4170$ mm (50 mm$\leq B < 100$ mm or 50 mm$\leq H < 100$ mm), and (iii) $L > 8340$ mm (B or $H > 100$ mm), where B and H are the width and height of the cross-section. However, and regardless of the value of L, the American standard limit ($L/240$ for open cross-sections and $L/400$ for closed cross-sections) is always less strict than the Chinese standard limit ($L/500$).

In resume, there are four major unsolved critical issues regarding the GIs of pGFRP profiles:

- Most data on GIs of pGFRP profiles is still in possession of pultrusion manufacturers, which do not share that information to public because of privacy issues (quality control and market competition).
- The number of available results of measurement of GIs is not sufficient for statistical treatment and reliability analysis. Furthermore, the measuring techniques are not yet standardized (like some standard methodologies for material characterization), which leads to a wide plethora of different approaches with distinct equipment and set-up (and inherent precision).
- The existing computational FE studies assume GI with critical buckling mode shapes and "steel-based" amplitudes [41–43,48,50, 52,53,56–58]. Of course, the adopted GI assumptions are often unrealistic and do not reflect the true behaviour of the structural member.
- The most relevant available structural standards or guidelines for the design of composite structures [59–63] do not reflect the level of GIs in their design curves for prediction of the strength of pGFRP members. In particular, the recent European Technical Specification CEN/TS 19101 [63] includes a strength curve with an empirical constant to account for GIs, but its value is fixed and does not vary with the GI magnitude.

The lack of recommendations for the consideration of GIs in the analysis and design of pGFRP structures is a key issue to solve within the next years. The establishment of accurate procedures to predict the strength of pGFRP members can only be reached if realistic GI shapes and amplitudes are known. Hence, this study aims to contribute to the development of a new methodology for the characterization of GIs of pGFRP members (shapes and amplitudes), which will enable (i) wider data sample, (ii) more accurate computational simulations and (iii) more reliable calibration of strength curves to be provided in structural design standards. The present study introduces a precise GI
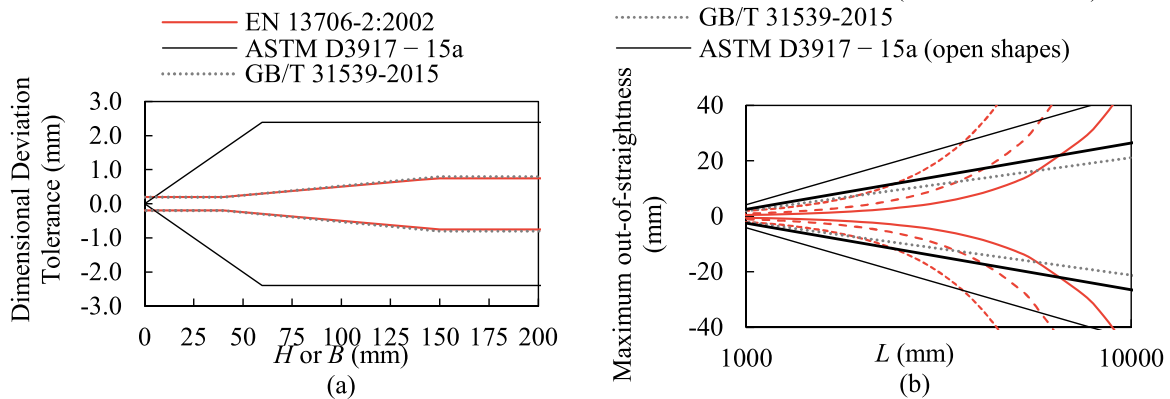

Fig. 1. Geometrical production requirements of standards EN 13706–2 [46], ASTM D3917–15a [30] and GB/T 3153 [55] for (a) DD of B and H and (b) GI tolerances associated to the out-of-straightness.

measurement methodology for pGFRP profiles, encompassing an experimental setup and the definition of key geometrical parameters (height, width, thickness and corner radius). Furthermore, the evaluation of point cloud transformations for shell-type nodes is conducted to improve the quantification of plate deformation modes. Fig. 2 shows a schematic representation of the proposed framework for obtaining the dimensional sizes and imperfections related to pure deformation modes. The proposed methodology is expected to yield comprehensive GI data for pGFRP profiles, enabling more accurate computational modelling, calibration of design curves, and reliability studies for determining partial safety factors.

2. GI measurement setup

A 3D contact CMM of the moving bridge type [64], manufactured by DEA Brown & Sharp and model GAMMA 2203, was used for the measurements, as shown in Fig. 3. The CMM offers a measuring volume of 1500 mm (x) × 1000 mm (y) × 1000 mm (z), as depicted in Fig. 4. It possesses a resolution of 0.0001 mm and a measurement accuracy of 0.010 mm, with a 95% confidence interval. This testing equipment is traceable to measurement standards which perform the measurement units according to the International System of Units (SI), at a controlled temperature of 20°C ± 1°C and relative humidity ≤ 65%..

The CMM consists of three main components, as depicted in Fig. 4. The first component is responsible for housing and facilitating vertical movement of the probe system along the z-axis. The second component is the moving bridge, which connects to the ram (part of the first component) and enables transverse movement of the ram along the y-axis. The third component is a stationary granite table that provides support for the moving bridge and allows it to travel along the longitudinal x-axis.

The probe system, which is attached to the first component as illustrated in Fig. 4, consists of an articulated system manufactured by Renishaw® PH10M Plus. This system incorporates a contact probe TP-20, which is a kinematic touch-trigger probe system. The stylus of the probe has specific dimensions, including a total length of 20 mm, a shaft diameter of 1.4 mm, an extension length of 10 mm, and a ruby ball tip with a diameter of 2 mm. The measurements conducted using the current setup follow the guidelines outlined by Flack [65], who provides recommendations to accurately quantify the measurements. In terms of the minimum number of measured points, the standard BS 7172 [66] suggests a minimum of three points to define a plane. In the case of the workpiece being examined, which consists of prismatic pieces with long wall segments, the points are distributed along cross-section segments, with a minimum of three points in each cross-section and each wall. This approach ensures a comprehensive measurement coverage and accuracy.

3. Point cloud transformation

The point discretization for profile characterization is established based on specific requirements and practical limitations, which include: (i) limiting the specimen length to a maximum of 1500 mm (defined based on the equipment available), (ii) maintaining a distance of 50 mm between each measured cross-section, (iii) ensuring a minimum of three points measured per cross-section wall, (iv) difficulty in obtaining accurate measurements of internal radius due to limitations in the ruby ball curvature for internal corners, (v) aligning the points measured on both faces of the same wall for thickness characterization, while also maintaining symmetry along the cross-section profile, and (vi) conducting three measurement series for each specimen to assess repeatability and, consequently, its contribution to the combined measurement uncertainty.

It should be noted that in a specimen with a length of 1500 mm, with 50 mm between each measured cross-section, the maximum number of cross-section measurements along the longitudinal length would be 30. However, due to the CMM's limitations in reaching the extremities where the boundary condition exists (as shown in Fig. 3-c and Fig. 5-a),
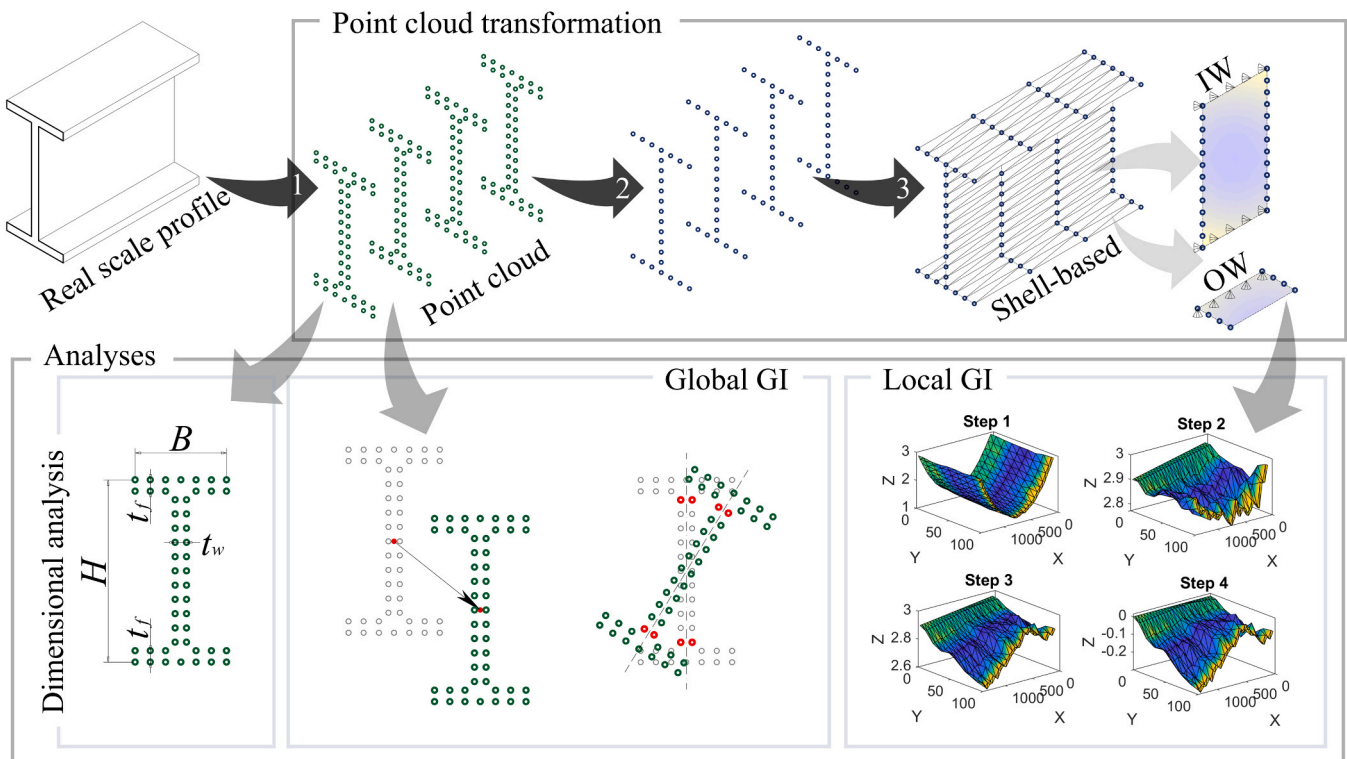

Fig. 2. Flowchart of the geometrical characterization method, illustrating the point cloud transformation and the three main types of analyses: dimensional deviation, global GI and local GI (t_f and t_w are flange and web thickness; IW and OW are internal and outstand wall).
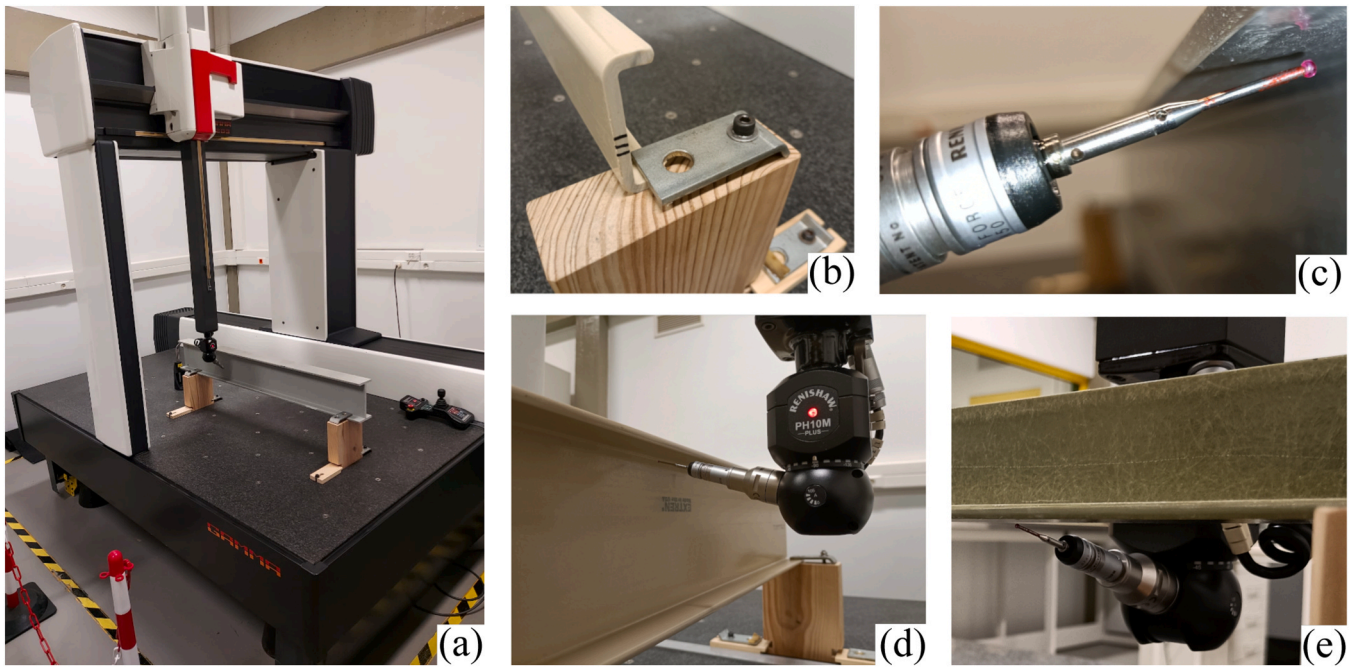
Fig. 3. Automatic DEA GAMMA 2203 3D CMM: (a) moving bridge, (b) boundary condition of a C-section profile, (c) detail of the stylus system in the measurement of an I-section, (d) detail of measurements under a C-section flange, and (e) under an angle section.
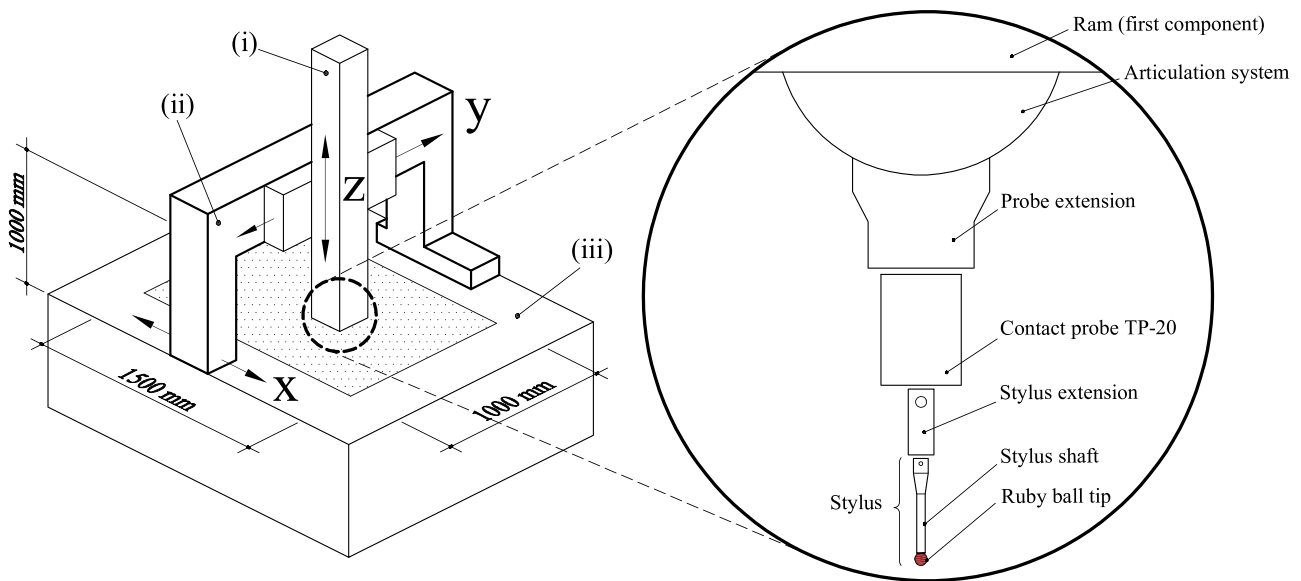

Fig. 4. Schematic description of the CMM, indicating the (i) ram, where the probing system is attached (in detail), (ii) moving bridge, and (iii) stationary table made of granite (adapted from ISO 10360–1:2000 [64]).

the number of cross-sections measured may be slightly less (i.e., $L < L_T$). Fig. 5 illustrates the point discretization along both longitudinal (length) and transversal (cross-section) directions.

The CMM provides raw data in the form of a four-column matrix. The first column contains a code that identifies the measured point, including the section, line, and point number. The section corresponds to the position along the longitudinal x-direction, the line denotes the planar face within that specific section, and the point number refers to the precise point on that line for each section. As an example, consider the point depicted in Fig. 5-b, for the I-section. If it is located within the 1st section, the code would be represented as: 010407 (1st section, 4th line, and 7th point). The remaining three columns represent the spatial coordinates along the x, y, and z axes (refer to Fig. 6-a). The

measurements are conducted on both faces of each wall of the profiles, ensuring comprehensive coverage of the profile's geometry (see Fig. 5-b). The measurement procedure is automatic, taking into account the profile's geometry, and achieves an average measurement speed of 10 points per minute (approximately 6 s per point), with variations depending on the complexity of the cross-section.

A shell-based point cloud was generated to capture the imperfections of the pGFRP profile and facilitate their incorporation into a computational model. This point cloud was constructed based on the measured data, which cover both faces of the cross-section. To create a new reference point cloud, the average location of each pair of points on opposing sides of the wall within the same profile section was determined (see Fig. 6-b). The thickness of each new point was measured as
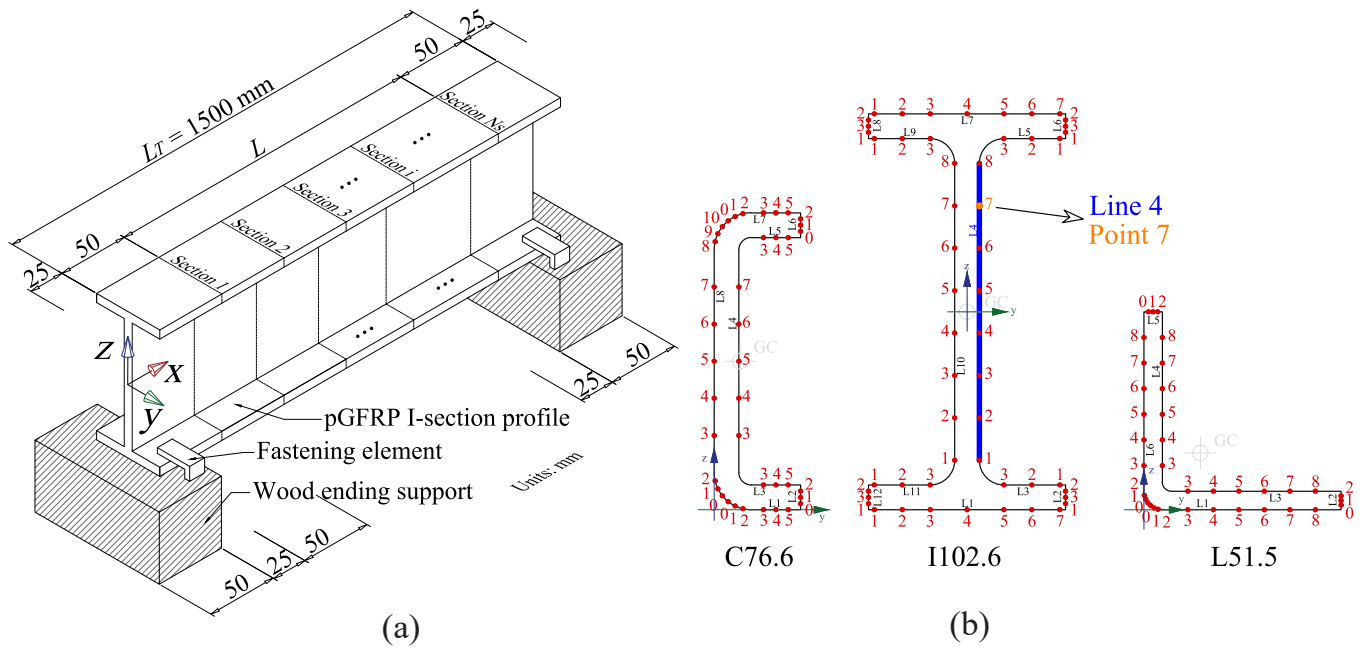
Fig. 5. Measured point location (a) along the longitudinal *x*-direction (section) and (b) in the cross-section plane for typical pGFRP open cross-sections (lines and point numbers).
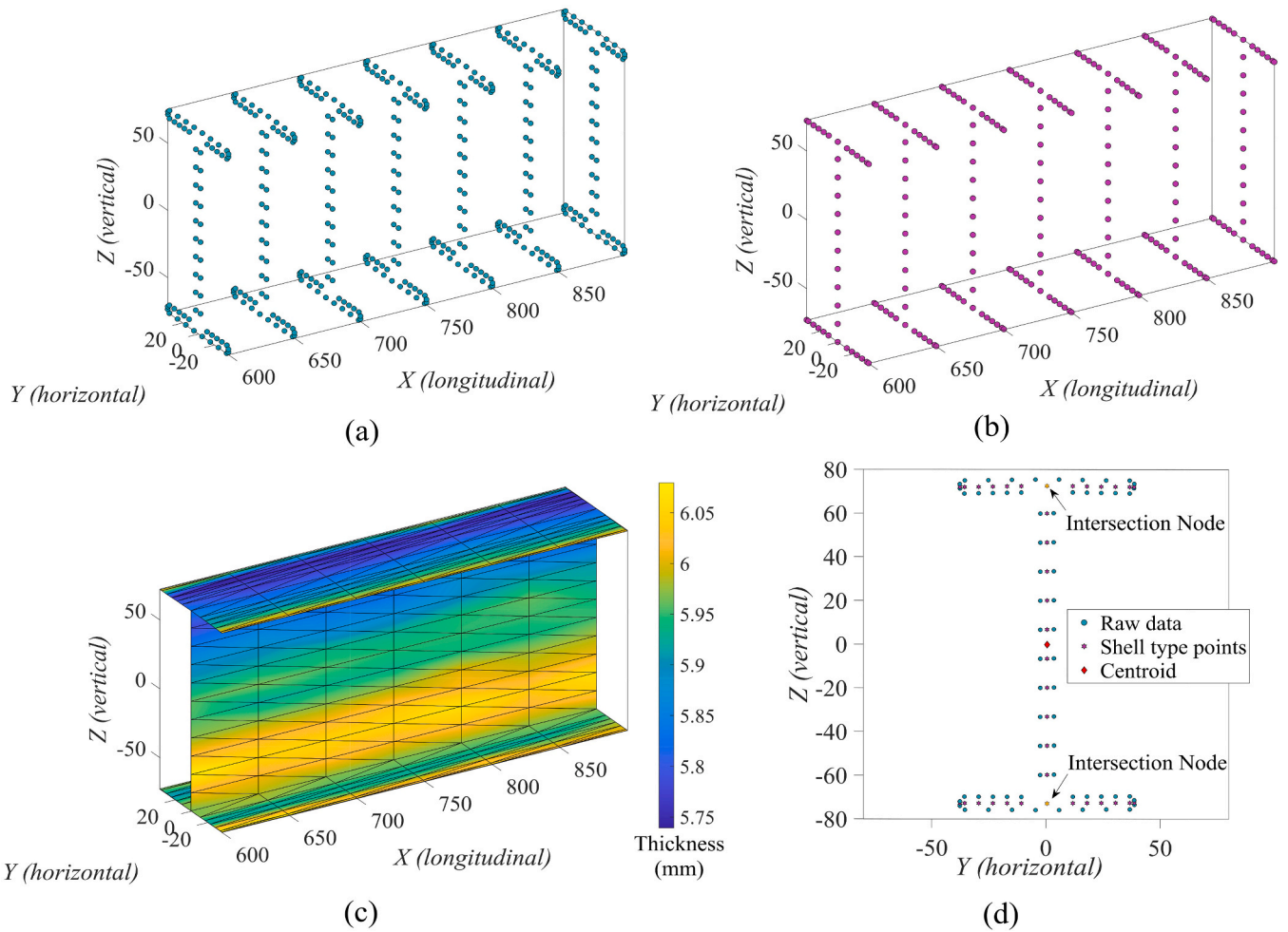

Fig. 6. Measurements of a pGFRP I-section: (a) raw data, (b) shell-type nodes, (c) shell-type surface with thickness colourmap, and (d) cross-section point description (measurements in mm).

the absolute distance between two locations on opposing sides of the wall, along with its new coordinate at the middle line of the profile. In cases where wall segments intersect within the cross-section, interpolation was employed to ensure continuity of the components along the cross-section. Similarly, due to the discontinuity along the longitudinal direction (the distance between each measured cross-section), the coordinates and thickness values were linearly interpolated using the neighbouring measurements between each section. Fig. 6-d provides a schematic representation of the transformation process, illustrating the raw data measured, the shell-type points, the intersection nodes, and the centroid of the recorded raw data, while Fig. 2 presents a flowchart of the three stages of the point cloud transformation. Fig. 7 displays a cross-sectional view of a wide-flange section, highlighting the GI using a thickness field colourmap. By employing this approach, the shape and amplitude of the GIs can be accurately quantified and incorporated into shell-based computational models, enhancing the understanding and analysis of the pGFRP profile's behaviour.

The assessment of repeatability in measurements is a crucial aspect of this study, which involve three repetitions for each tested specimen. The repeatability uncertainty component is determined by calculating the Euclidean norms between each repetition within the same specimen. In simpler terms, the distance between each measured point for each repetition is computed, considering a three-dimensional Euclidean space $\mathbb{R}^3$. Fig. 8 provides a schematic perspective, illustrating the presence of repeatability uncertainty in the measurements of 3480 points (1160 per repetition) of a C-section. The figure depicts the full-section measurements (Fig. 8(a)), the distances d_{12}, d_{13} and d_{23}, and the distribution of these distances. This analysis allows for the quantification of repeatability and its impact on the overall measurement results.

The data obtained from the measurements allowed the extraction of relevant outputs, including dimensional deviations (DD) and geometric imperfections (GI). The dimensional analysis was focused on the determination of the sizes of the profile, such as height, width, thickness, and corner radius. Regarding the GIs, two primary categories were identified: global GIs and local GIs. The global GIs refer to the overall deviation of member longitudinal axis ("rigid-body" deformation of the cross-section) and includes the following categories: (i) minor-axis GI, which involves global deviations along the minor-axis (weak axis) of the profile, (ii) major-axis GI, which pertains to global deviations along the major-axis (strong axis) of the profile, and (iii) twist GI, which represents torsional rotation of the profile. On the other hand, local GIs refer to defects associated to in-plane deviations of cross-section walls (the member longitudinal axis remains undeformed) and includes the following categories: (i) GI of simply-free supported plate (outstand wall), which applies to the flanges of an I-section, and (ii) GI of simply-simply supported plate (internal wall), which applies to the web of an I-section.

4. DD procedure

The current approach presents a comprehensive methodology to determine the various sizes and parameters of pGFRP profiles, including height (H), width (B), thickness (t), and corner radius (R). The height (H) was determined as the vertical distance of the profile, perpendicular to its primary axis. The width (B) was determined perpendicular to the minor-axis (orthogonal to the height direction), providing the transverse size of the profile. The thickness (t) was determined at multiple points along the cross-section, ensuring that each measured point has a corresponding opposing point in the same wall. This enables a comprehensive assessment of the wall thickness variation across the profile. For pGFRP profiles with external round corners, such as L-sections, C-sections, and tubular sections, the corner radius (R) was determined using the Pratt technique [67], which involves fitting a circle to accurately define the corner curvature.

To assess the DD, the measured sizes were compared to the nominal values provided by the profile's manufacturer. The DD was calculated as the relative difference between the measured and nominal values. It is important to note that the DD analysis was based on the reference points indicated in Fig. 9, and the DDs were derived directly from the raw measurements without considering measurement uncertainties.

Fig. 10 illustrates boxplots representing the DDs determined for an angle section, serving as an example of the resulting outcome. These boxplots provided a visual representation of the deviations between
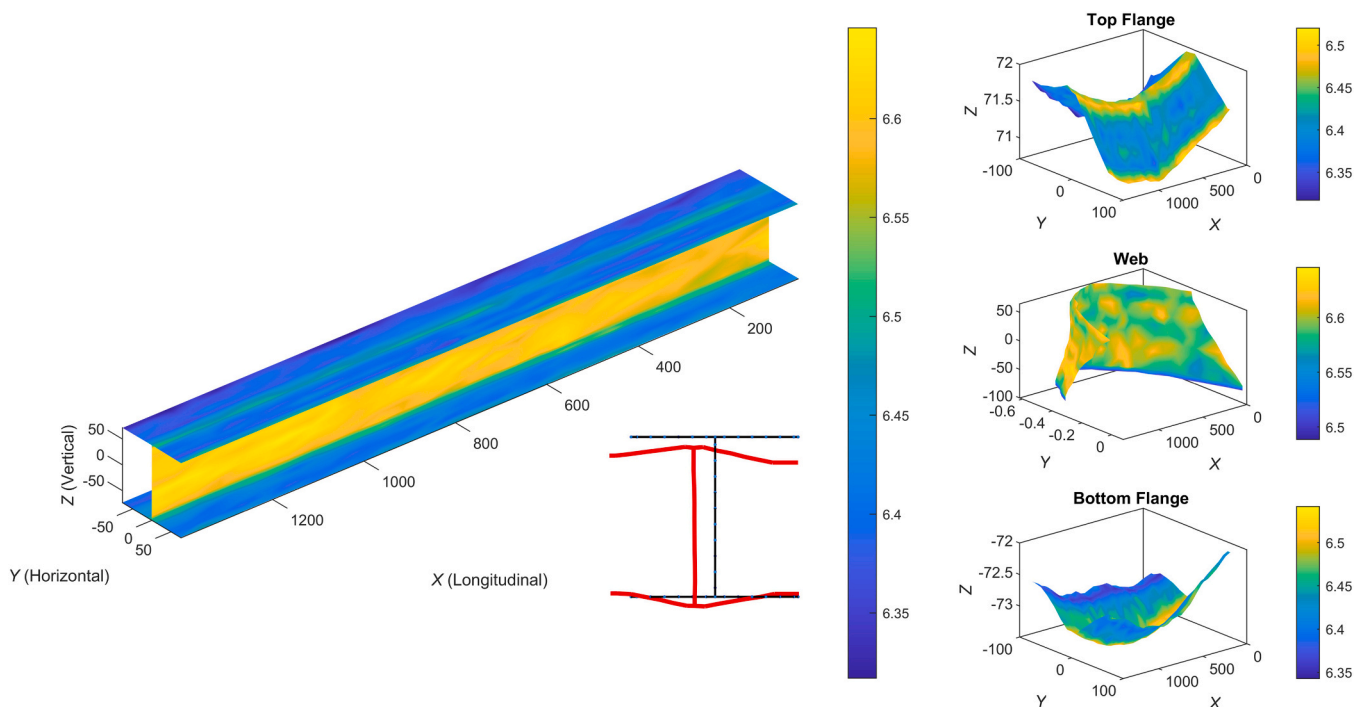

Fig. 7. 3D shell-type element imperfected shape for a wide flange Sections (W152.6–2) with thickness colourmap (measurements in mm and 2D shape at mid span amplified 20 times).
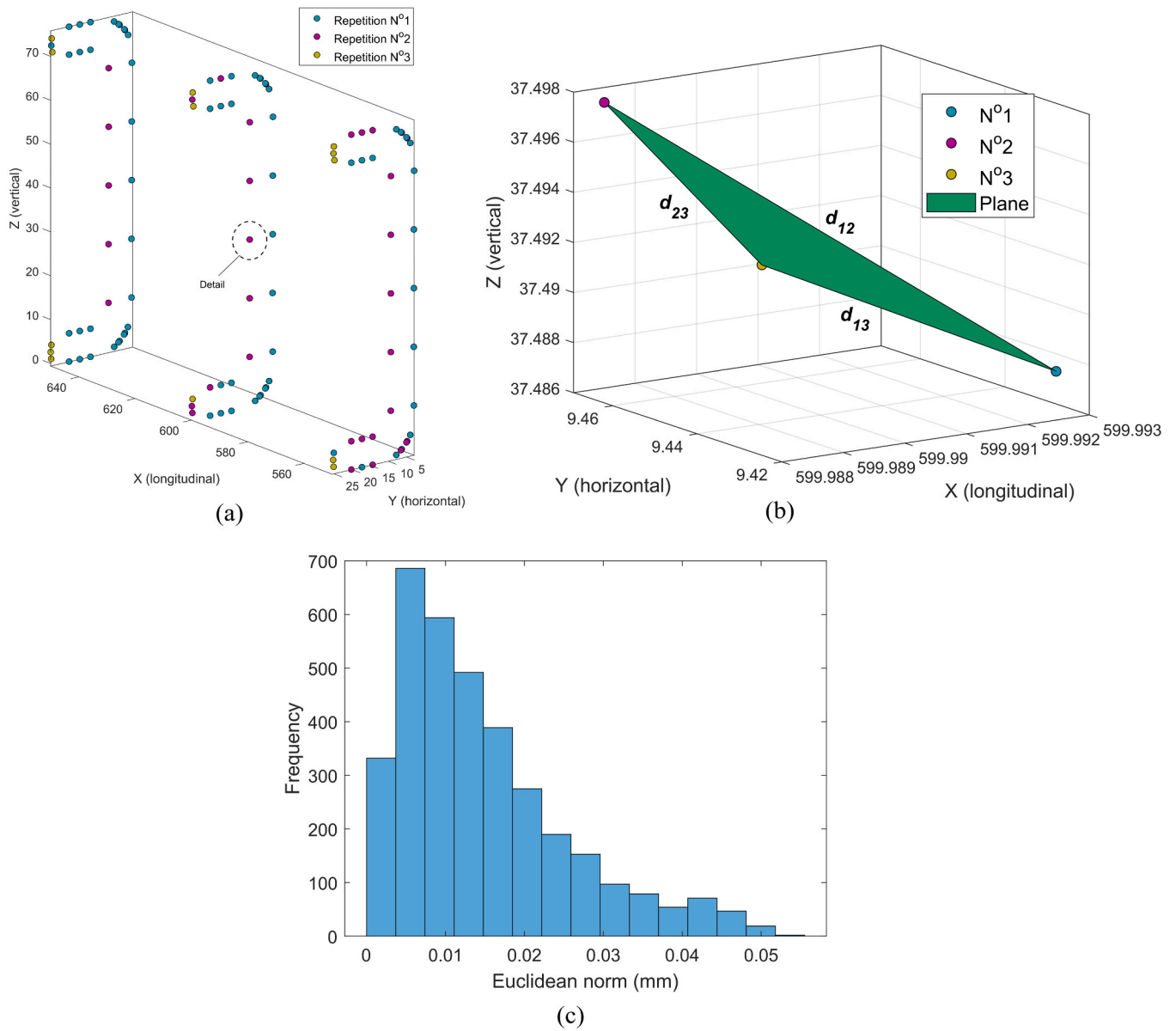
(a)

(b)

(c)

Fig. 8. Illustration of the repeatability uncertainty component in the repetition of the measurements in a C-section with 1160 measured points: (a) full-section measurements, (b) detail of the plane and distances of each repetition in the measurement of one point and (c) distribution of the Euclidean norms of all repetitions in one specimen.

each measured size and the reference distances depicted in Fig. 9. In the boxplots, each data point corresponds to a specific property measured along the longitudinal length of the profile. The boxplot displays key statistical measures that summarize the distribution of the DDs. These measures typically include the median, which represents the central tendency of the data, as well as the lower and upper quartiles, which indicate the scatter. For the thickness DD, it is possible to depict the 5th and 95th percentiles along the cross-section for both wall segments (t_1 and t_2). These percentiles provide insight on the variation of thickness along the profile, specifically highlighting the range within which 90% of the measured thickness deviations lie.

5. GI procedure

5.1. Modal Decomposition of GIs

The GIs were derived from a generalized deformation mode via an indirect technique. Overall, a general GI of a prismatic structural

member (G_m) is the combination of several GI components associated to pure deformation modes, given by

$$G_m = \underbrace{\alpha_{FM}\Phi_{FM} + \alpha_{Fm}\Phi_{Fm} + \alpha_t\Phi_t}_{global\ modes} + \underbrace{\alpha_\ell\Phi_\ell}_{local\ modes} \quad (1)$$

where G_m is the generalized GI represented by the measured points, Φ and α are the shape and amplitude of each pure deformation mode, respectively. The cross-sections considered in this analysis exhibit two fundamental types of deformation modes associated with their buckling behaviour, namely global and local modes (as detailed in Table 1). The global modes include major-axis flexural mode (Φ_{FM}), minor-axis flexural mode (Φ_{Fm}), and twist mode (Φ_t). These modes capture the overall bending and twisting behaviour of the cross-sections. On the other hand, the local modes are characterized by a single cross-sectional shape (Φ_ℓ) and include two types: outstand walls (OW) and internal walls (IW). For instance, C-sections consist of two OWs and one IW, resulting in a single local deformation mode composed of the OW and IW modes. Fig. 11
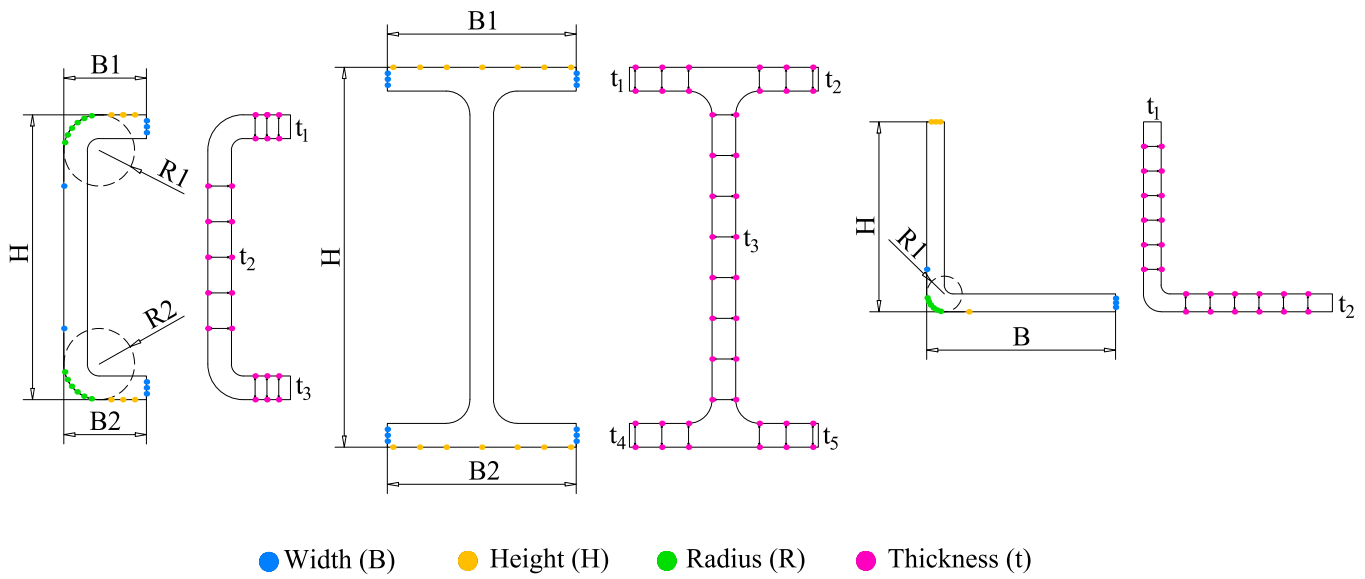
Width (B)   Height (H)   Radius (R)   Thickness (t)

Fig. 9. Reference points used for the dimensional measurements of the C, L, and I-sections in accordance with the reference points in Fig. 5.
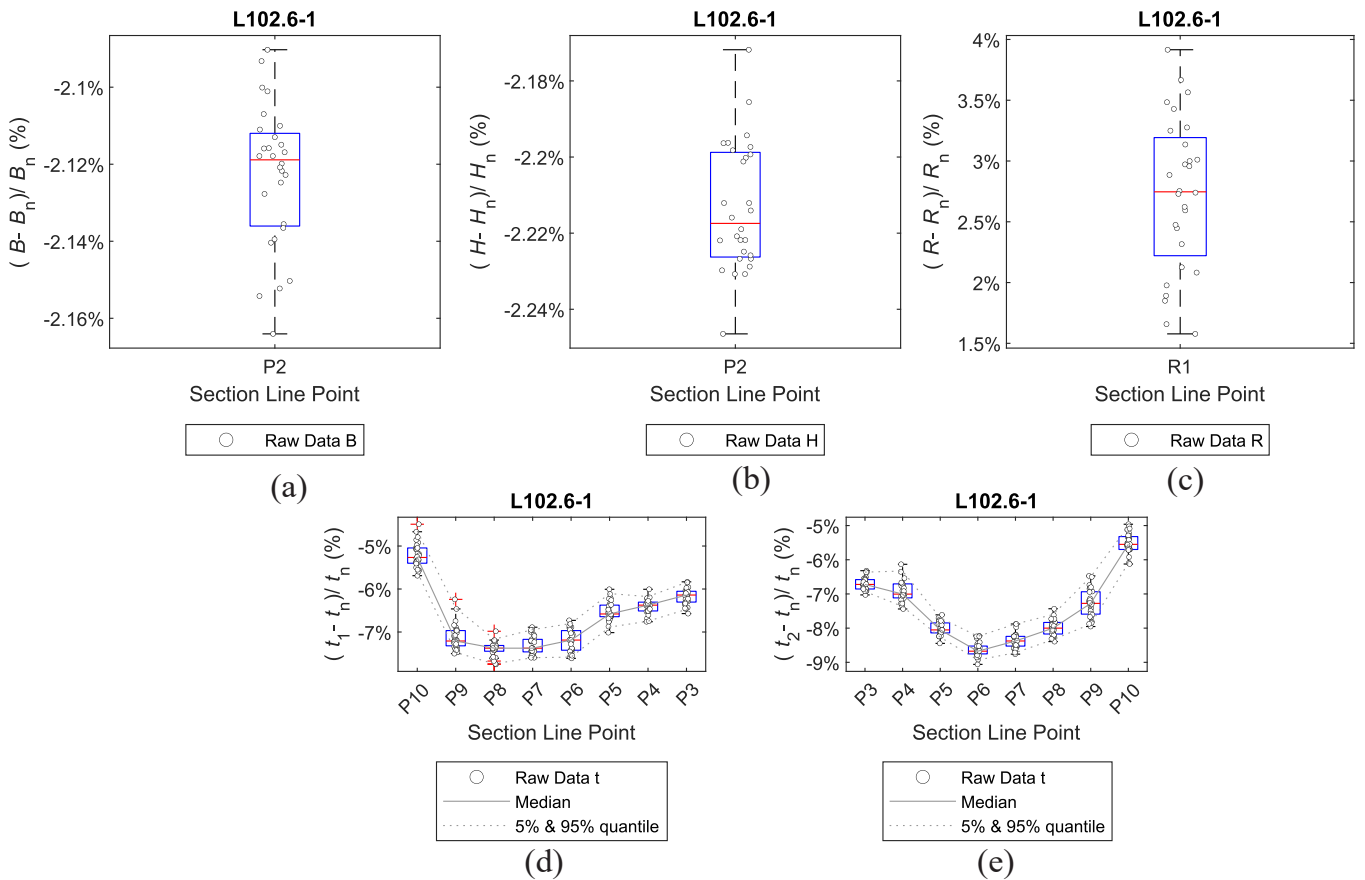
Fig. 10. Typical dimensional deviation results for an angle section: (a) height, (b) width, (c) corner radius, (d) thickness of the vertical wall, (e) thickness of the horizontal wall.

provides visual representations of the deformation modes for common pGFRP cross-sections.

5.2. Global GI

Fig. 12 illustrates the vector form of a linear algebraic technique used to determine the global geometric imperfection (GI) flexural modes. The procedure involved several phases:

(i) *Calculation of the centroidal axis*: The centroidal axis of the member was computed by taking the average coordinate of the points in each measured cross-section using the raw data. The spatial coordinates of each centroid were determined as the sum of the translation vector (r) from the original CMM coordinate

Table 1

Definition of the GIs based on current standards: EN 13706–2 [46], ASTM D3917 [30] and GB/T 31539 [55].

| Buckling Mode Category	Geometric Category	GI Designation	Standards		
			EN 13706-2	**ASTM D3917**	**GB/T 31539**
Global	Member	Minor-axis GI	Straightness	Straightness	Straightness
		Major-axis GI	Straightness	Straightness	-
		Twist GI	Twist	Twist	-
Local	Cross-section	Internal wall GI	Flatness in transverse direction	Flatness	Web Flexure
		Outstand wall GI	Size of angle	Angularity	Flange Inclination
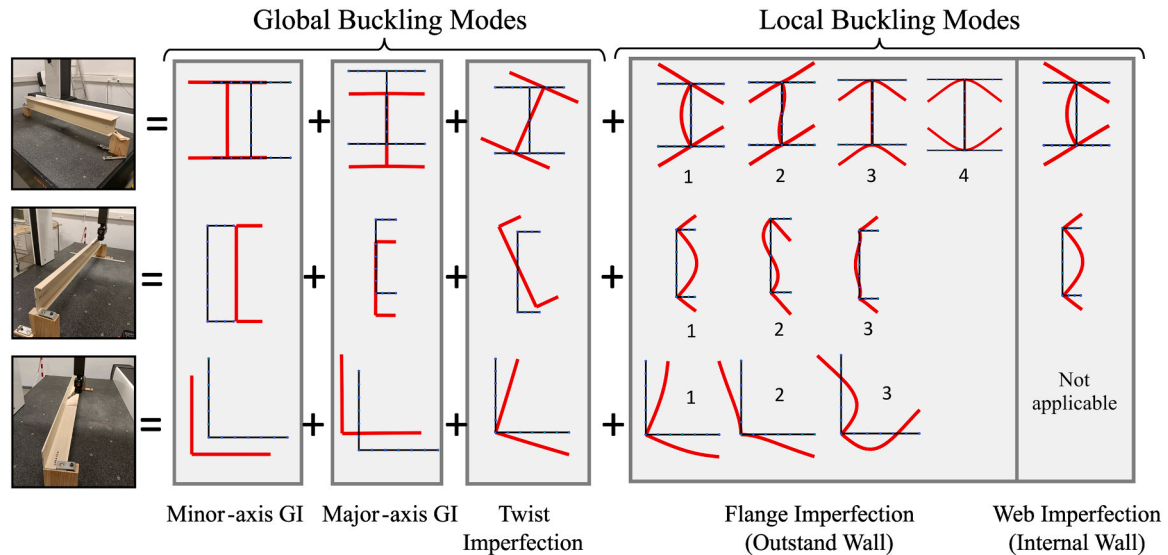
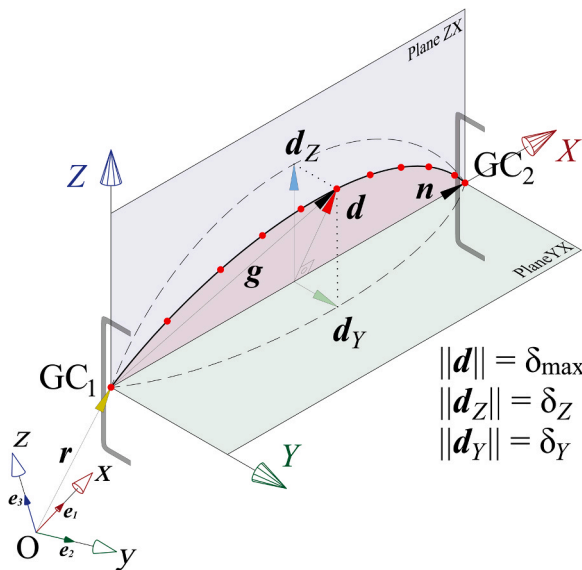**Fig. 11.** Deformation modes configuration for I, C and L sections.

Fig. 12. Illustrative description of the extraction of the flexural deformation modes represented by the vector **d**.

system (*xyz*) to the new orthogonal coordinate system (*XYZ*), and the cross-section vector (**g**) originating from the first cross-section centroid.

(ii) *Creation of the align vector*: From the coordinates of the centroids obtained from the extreme cross-sections, an align vector named **n** was formed.

(iii) *Calculation of the flexural deformation mode vector*: An algebraic approach was employed to obtain the vector **d**, which is perpendicular to **n** and reaches the nearest gravity center. This vector **d** represents the flexural deformation mode and has components in the *Y* and *Z* directions, corresponding to the minor-axis and major-axis flexural modes, respectively.

The mathematical expressions for calculating the minor-axis flexural GI (δ_z) and the major-axis flexural GI (δ_y) are given by

$$\delta_Z = \|\boldsymbol{d}_Z\| = \left\| \boldsymbol{g}_{ZX} - \left(\frac{\boldsymbol{g}_{ZX} \cdot \boldsymbol{n}}{\|\boldsymbol{n}\|} \right) \frac{\boldsymbol{n}}{\|\boldsymbol{n}\|} \right\| \tag{2}$$

$$\delta_Y = \|\boldsymbol{d}_Y\| = \left\| \boldsymbol{g}_{YX} - \left(\frac{\boldsymbol{g}_{YX} \cdot \boldsymbol{n}}{\|\boldsymbol{n}\|} \right) \frac{\boldsymbol{n}}{\|\boldsymbol{n}\|} \right\| \tag{3}$$

where $\boldsymbol{g}_{ZX}$ and $\boldsymbol{g}_{YX}$ represent the projections of each cross-section vector originating from the first cross-section gravity centre onto the *ZX* and *YX* planes, respectively.

The extraction of the twist deformation mode is carried out independently of the flexural modes and involves determining the rotation of the full cross-section about the shear centre along the member length. The twist mode was extracted based on the rotation of the web (either for C or I-sections), as described by Selvaraj [13] for cold-formed steel profiles. The rotational twist was calculated by performing a linear curve fitting using MATLAB's built-in *polyfit* function [68]. This function provides the best polynomial curve fitting of the general form $p(y) = p_1 y^n + p_2 y^{n-1} + \ldots + p_n y + p_{n+1}$, using a least-square technique. Fig. 13 illustrates a schematic representation of the twist reference planes and points. For I- and C-sections, a one-degree curve ($n = 1$) was fitted with four measured points near the web-flange junctions. In case of angle sections, all points along the wall components were used for the
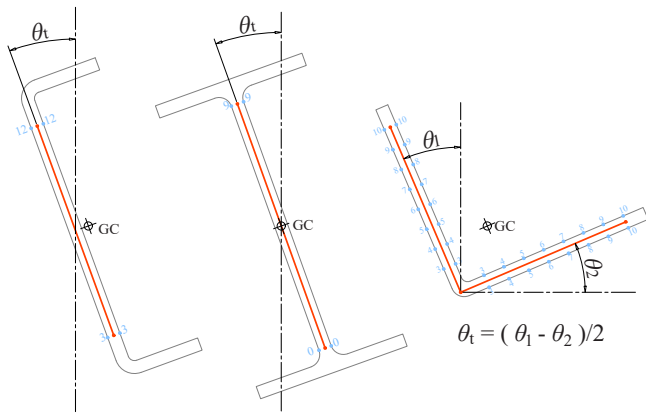
Fig. 13. Twist reference points and planes for C, I and L-sections.

one-degree curve fitting. It is important to note that for angle sections, the twist mode is combined with the local deformation mode, as shown in Fig. 11. The angle of twist (θ_t) can be derived as $\theta_t = (\theta_1 - \theta_2)/2$, where θ_1 and θ_2 represent the twist angles of each wall segment.

The variation of the global GIs along the member axis are provided in Fig. 14 for three "equal" specimens (M1, M2 and M3), showcasing two significant aspects of GI characterization: (i) deformation shape and (ii) maximum amplitude. The results shown in Fig. 14-a,b illustrate the typical shape of the flexural GIs in a C-section, exhibiting a single half-wave shape, following the form of $\alpha sin(\pi X/L)$, where α is the maximum amplitude measured. This indicates that the member experiences an initial eccentricity along its major and minor axes, resulting in an initial 3D curved shape. In this specific case, the variation of the twist GI along the member axis of a wide-flange section (illustrated in Fig. 14-c) is almost linear (note that other profiles may not show this linear trend). The differential twist rotation between the extreme values in the 1.35 m long measured member leads to an average twist per unit of length equal
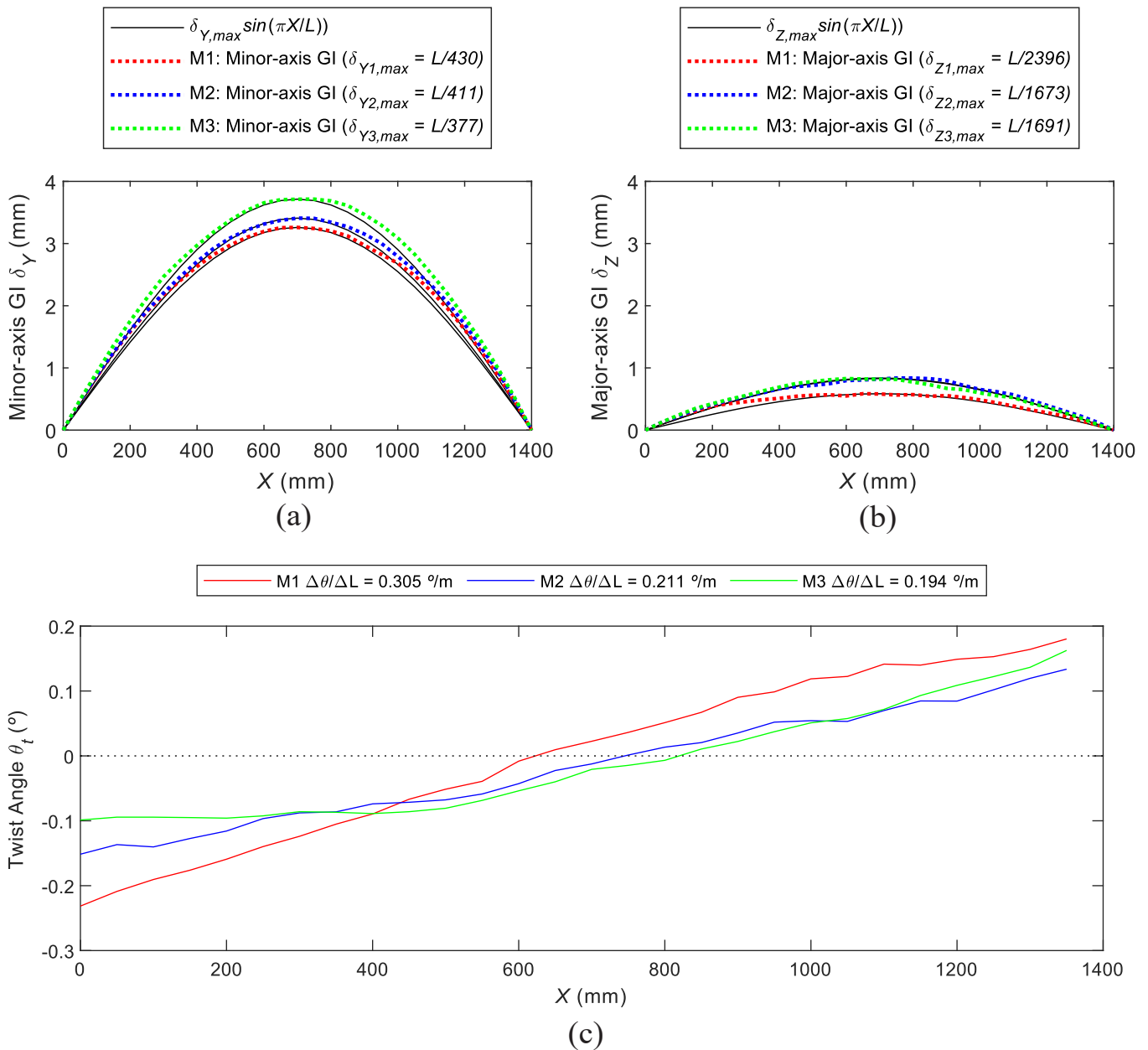

(a)

(b)

(c)

Fig. 14. Typical results of global GIs measured for three specimens (M1, M2 and M3): (a) minor-axis GI of a C-section, (b) major-axis GI of a C-section, and (c) twist GI of a wide-flange section.

to 0.24°/m, which is considered a low value based on the manufacturing limits set in ASTM D3917–15a [30] (3.28 °/m).

5.3. Local GI

As described by Eq. (1), a general GI of a member can be represented as a combination of pure deformation modes. By removing the flexural and twist GIs from the overall measured GI of the member, it becomes possible to identify the local GI. This procedure involves treating each wall as an independent element and considering the influence of intermediate nodes within each wall segment. Flange elements consist of OW segments with a single intersection node, while web elements comprise IW segments with two intersection nodes. The longitudinal edge points of IW segments are treated as simply-supported, whereas only the points near the junction with other walls are simply-supported in OW wall segments.

The extraction of the local GI followed the step-by-step procedure outlined in Fig. 15, which comprises four main steps: (i) shell-type transformation involving the identification of intersection nodes and wall segments, (ii) decomposition of the flexural GIs (minor- and major-axis), (iii) decomposition of the twist GI, and (iv) extraction of the local GI within the orthogonal coordinate system (xyz) through alignment and translation (centering).

Section 3 outlined the initial stage (step 1) of the process, which involved transforming the raw measured data into shell-type elements. The shell-type points (p_1) were organized into a matrix structure, which was rearranged based on the cross-section, wall segments, and points. In the second phase (step 2), the subtraction of the flexural GIs was performed. This process is defined by

$$p_2 = p_1 - d \tag{4}$$

which subtracts the flexural vector d (as illustrated in Fig. 12) for each cross-section, from each shell-type points vector p_1 (given for each cross-section, wall element and point). The third step involved the subtraction of the twist GI, as described by

$$p_3 = p_{2I} + (p_2 - p_{2I})R_x|_{\alpha=-\theta_t} \tag{5}$$

$$R_x(\alpha) = \begin{bmatrix} 1 & 0 & 0 \\ 0 & \cos\alpha & -\sin\alpha \\ 0 & \sin\alpha & \cos\alpha \end{bmatrix} \tag{6}$$

where p_{2I} is the vector point from step 2 located at the intersection node; p_2 is the vector point from step 2; R_x is the rotational matrix around the x-axis by α; and θ_t is the twist angle. This procedure requires two pieces of information: (i) a reference point for rotating the wall element and (ii) the twist angle. The reference point is defined as the coordinate of the junction point of the wall segment, p_{2I}, obtained in step 2, for each cross-section and wall, but for the point located at the intersection point. For OW wall elements, the intersection point defined at the junction of the orthogonal walls (as shown in Fig. 6-d) serves as the rotational reference point. For IW elements, the rotational reference point is the gravity centre of the points involved in the twist mode extraction (refer to Fig. 13). The twist angle for each cross-section (θ_t) is obtained from Section 5.2 and applied as a rigid body rotation around the x-axis with a negative twist angle, using Eq. (6) as the rotation matrix around the x-axis.

The output after the second and third steps is the local GI[2] (step 4). However, due to the misalignment of the profile during measurements in the CMM, the resulting deformation mode is not centred or aligned in the x-direction, as depicted in Fig. 15, step 3. To address this issue, an alignment correction is performed using the Euler-Rodrigues' rotation formula [69,70], which provides an analytical equation for rotating a vector (s) around a given axis (u) by an angle of rotation (ϕ), as illustrated in Fig. 16-b. Considering the three-dimensional Euclidean space $\mathbb{R}^3$, the matrix form of the Euler-Rodrigues' rotation formula is represented by

$$p_4 = u(u \cdot s) + \cos\phi(u \times s) \times u + \sin\phi(u \times s). \tag{7}$$

where the vector point p_4 is obtained by multiplying the Euler-Rodrigues' equation by the vector s, which represents the reference vector to be rotated around the axis vector u by an angle ϕ (Fig. 16). The vector s is defined as the vector from the intersection point at the first cross-section ($i = 1$), obtained in step 2, to each measured point in step 3. Fig. 16 illustrates the procedure in a vector form.

The expressions for s and u are given by,

$$s = p_3 - (p_{2I})_{i=1} \tag{8}$$

$$u = \frac{e_1 \times n}{\|e_1 \times n\|} \tag{9}$$

$$n = (p_{2I})_{i=N_S} - (p_{2I})_{i=1} \tag{10}$$

where p_3 is the vector point from step 3, $(p_{2I})_{i=1}$ is the vector point from step 2 located at the intersection node at the first cross-section and vector u is defined as the unit vector (Eq. (9)), which is perpendicular to the plane formed by the canonical base vector e_1 and the vector n, calculated as the difference between the coordinates of the first and last points ($i = 1$ and $i = N_s$) at the intersection point from step 2 (p_{2I}), as given by Eq. (10), and graphically illustrated in Fig. 16-a. The calculation of u involves taking the cross product between these two vectors and normalizing the result by its magnitude.

Once the vectors u and s are determined, the rotation angle ϕ between the vectors n and the canonical base vector e_1 is calculated by means of

$$\phi = -\arccos\left(\frac{n \cdot e_1}{\|n\|}\right) \tag{11}$$

where e_1 is the canonical base vector and n is the vector defined according to Eq. (10). It is important to note that the angle ϕ should be negative because it represents the alignment process where the point may rotate in the opposite direction from its original position. This is consistent with the approach used for extracting the twist GI, as previously shown in Eq. (5).

The local GI is analysed separately for each wall segment, considering the predefined boundary conditions for IW and OW segments. Fig. 17 depicts a representative example of a local GI pattern of a C-section. The figure showcases the three-dimensional shape of the GI for each wall segment, visualized using a colormap that represents the mapped thickness field. Additionally, the image shows the GI pattern along the two-dimensional axes, specifically in the longitudinal (x) and transverse (y or z) directions.

---

[2] Apart from the well-established global and local imperfection deformation modes, an imperfected geometry comprises high degree of randomness deformation modes. When the global modes are removed from an imperfected shape, what remains is a combination of local modes and "other" higher-order modes that are challenging to categorize. These "other" modes can include shear and transverse extension modes that can be categorized by numerical procedures [81,82], but also deformation modes that have no clear identification. Moreover, these "other" modes have residual practical significance and thus are not considered.
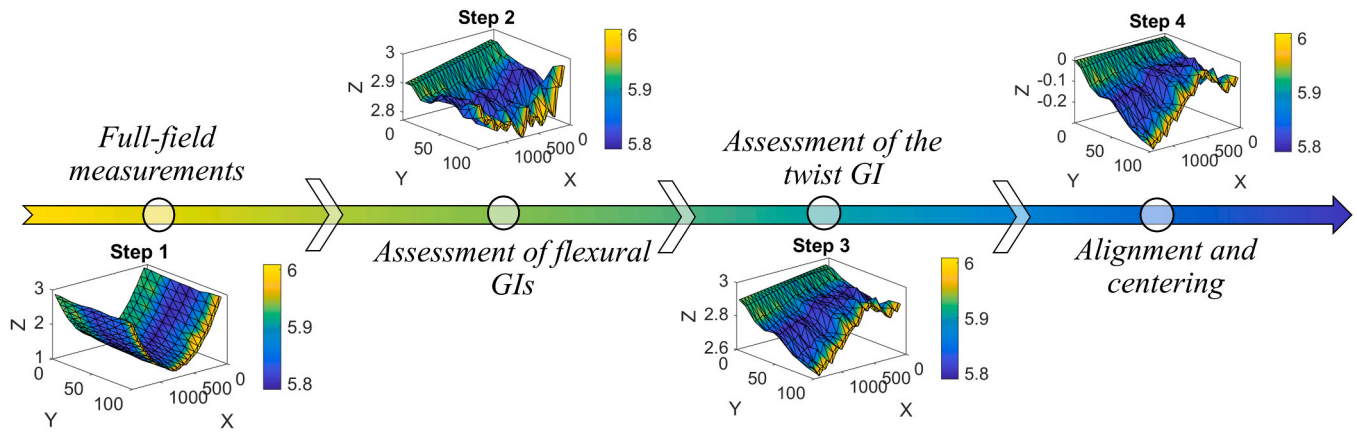
Fig. 15. Schematic illustration of the step-by-step procedure for extraction of the local GI, on a horizontal wall ("flange") of an angle section.
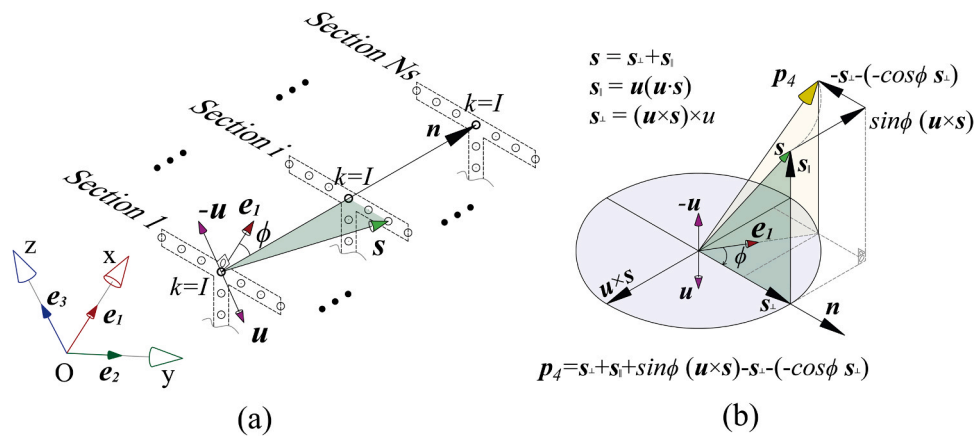

Fig. 16. Illustration of the Euler-Rodrigues' formula applied in the alignment of shell type points: (a) vectors in the ith cross-section and (b) graphical derivation.

6. On the influence of measured GIs on the strength of pGFRP profiles

As we stated before (Section 1.2), in the absence of more realistic information, many computational analyses consider GIs in the shape of the first buckling mode and mostly unbased amplitudes. In order to evaluate the methodology of the measured geometry (DD and GI) proposed in the present paper, a FE simulation of the real scale as-measured specimen W152–6-2 (illustrated in Fig. 7) under pure compression was performed considering geometrical and material nonlinear behaviours, and with GIs included. The specimen W152-6-2 is an H-section with nominal height and width of 152.4 mm, wall thickness of 6.35 mm and length of 1350 mm. The pGFRP material contains a vinyl ester resin, UV inhibitor and flame-retardant additives, from the 625 series produced by Strongwell [71]. The computational model was developed in Abaqus software [72], with the following features:

(i) The material is considered orthotropic and its elastic mechanical properties are illustrated in Table 2, which were based on experimental tests on coupons extracted from the walls of a profile from the same manufacturer and series (G_{xz} and G_{yz} were estimated on the basis of measured G_{xy}). The strength mechanical properties are indicated in Table 3, which were experimentally measured (the exception is f_{yz}, which was assumed equal to f_{xy}). The damage progression is simulated using the fracture energies indicated in Table 4. For $G_{x,t}$ and $G_{x,c}$ a typical value of 100 N/mm is reported in the literature [73]. The values of $G_{y,t}$ and $G_{y,c}$ were assumed equal to 160 N/mm and 42 N/mm, respectively, following the experimental values obtained by

Almeida-Fernandes et al. [74,75] for a pGFRP profile with similar mechanical properties. The material of the web-flange junction was the same of the flats parts (webs and flanges) and delamination failure was not considered.

(ii) The FE mesh is composed of quadratic elements: 6-node triangular (STRI65) and 8-node quadrilateral (S8R) shell finite elements, with a size control limitation of 5 mm resulting in a total of 60 014 finite elements.

(iii) The boundary conditions correspond to fixed support sections, one being fully fixed in all degrees-of-freedom, while the other is fixed except for the axial displacement, which is allowed.

(iv) The loading includes a compressive axial force applied to the centroid by using a multi-point constraint (MPC) connected to each point of the extreme section that is free to move axially.

(v) The solver of the non-linear analysis is the arch-length method (the modified Riks method [76]). The incremental-iterative method with mixed displacement and force control has an automatic incrementation with an initial arch length of 0.001, and minimum and maximum arch length of 1×10^{-30} and 0.01, respectively. The maximum number of increments is limited to 10000.

(vi) Regarding the material non-linear behaviour, it is worth mentioning that the failure mechanism is predicted using the Hashin [77,78] damage initiation criterion. The viscosity coefficient for damage stabilization was assumed as $\mu = 10^{-4}$, a value that was also adopted by Duarte et al. [79] and Lopes et al. [80].

(vii) The computational model considers the GI and DD of the W152-6-2 specimen (see Fig. 7). The GI is considered by means of the initial coordinates of the shell-type nodes given from the point
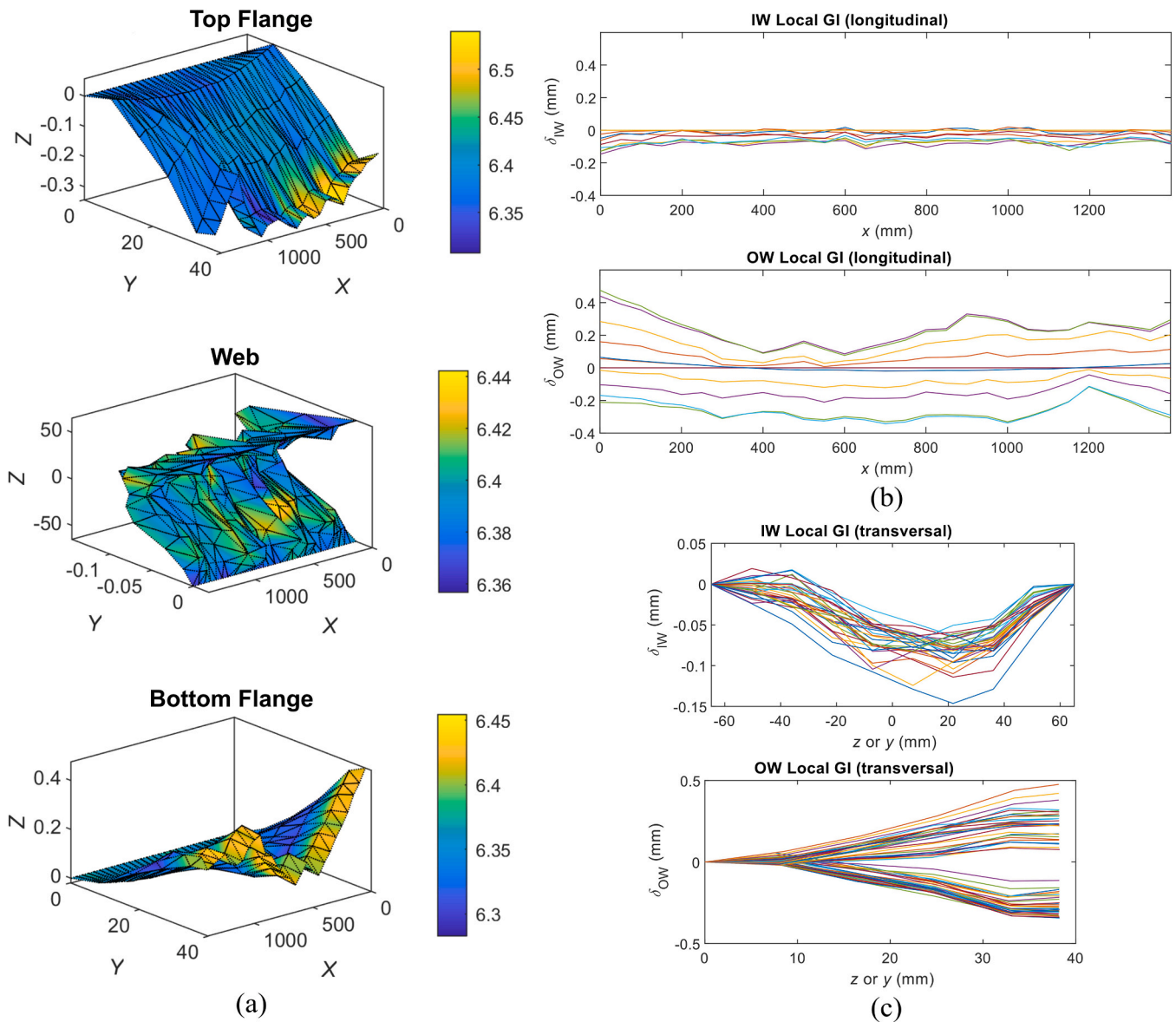
Fig. 17. Local GI in a C152.6 section (a) 3D local deformation mode, (b) local GI along the longitudinal direction and (c) local GI in transversal direction.

Table 2
Elastic properties of pGFRP W152–6 orthotropic material (x is the longitudinal direction, y is the transversal direction and z is the out-of-plane direction).

Elastic properties						
Wall	E_x N/mm²	E_y N/mm²	ν_{xy}	G_{xy} N/mm²	G_{xz} N/mm²	G_{yz} N/mm²
Flange 1	23978	12028	0.348	4430	4430	2215
Flange 2	26615	12170	0.358	4234	4234	2117
Flange 3	25995	11722	0.358	3633	3633	1817
Flange 4	25781	12231	0.359	3682	3682	1841
Web	25822	13281	0.341	3808	3808	1904

Table 3
Strength properties of pGFRP W152–6 orthotropic material (x is the longitudinal direction, y is the transversal direction, z is the out-of-plane direction, t denotes tension and c denotes compression).

Strength properties (N/mm²)						
Wall	$f_{x,t}$	$f_{x,c}$	$f_{y,t}$	$f_{y,c}$	f_{xy}	f_{yz}
Flange 1	407	499	93	193	116	116
Flange 2	420	547	93	182	114	114
Flange 3	389	542	93	194	113	113
Flange 4	435	516	93	182	107	107
Web	417	487	93	200	109	109

cloud transformation. The GI is inserted in the model using an analytical mapped thickness field, with nodal distribution, i.e., the geometrical model considers the thickness variation along each measured shell-type point. The GI of this model has a maximum amplitude of 0.418 mm ($L/3230$) for the major-axis GI, 0.427 mm ($L/3162$) for the minor-axis GI, 0.21°/m for the twist GI, 0.82 mm ($0.13 \cdot t$) for the OW GI (flanges) and 0.05 mm ($0.008 \cdot t$) for the IW GI (web). The real shape of the GI is depicted

in Fig. 7, while an amplification of the decomposed modal GIs is illustrated in Fig. 18. Regarding the sizes of the section geometry, it has an average value of 150.91 mm for the height, 152.39 mm for the width, 6.60 mm for the web thickness and 6.42 mm for the flange thickness.

Three models were considered in the analysis. The "true" model (TM) was the model comprising the real GIs and measured dimensions. The

Table 4

Fracture energies of pGFRP W152–6 orthotropic material (x is the longitudinal direction, y is the transversal direction, t denotes tension and c denotes compression).

Fracture energies (N/mm)				
Wall	$G_{x,t}$	$G_{x,c}$	$G_{y,t}$	$G_{y,c}$
Full section	100	100	160	42

other two models were designated nominal models (NM), as they consider the nominal geometry provided by the manufacturer (W $152.4 \times 152.4 \times 6.35$ mm^3) and GI with the shape of the first critical buckling mode with two distinct amplitudes: $0.13 \cdot t$ and $0.004 \cdot t$ ($t = 6.35$mm, the nominal thickness of the profile) – models NM $0.13 \cdot t$ and NM $0.004 \cdot t$, respectively. The amplitude of $0.13 \cdot t = 0.82$mm was chosen based on the maximum measured local GI of 0.82 mm. The amplitude of $0.004 \cdot t$ was found by a trial-and-error procedure only for numerical purposes: it was high enough to avoid following the trivial path and changing path for the bifurcation (buckling) load, but also sufficiently small to avoid significant influence on the post-buckling mode shape of the column.

Fig. 19 presents the variation of the applied-to-critical load ratio with the axial shortening for the three models (TM, NM $0.13 \cdot t$, NM $0.004 \cdot t$). For low levels of compression up to the onset of local buckling (mode shape with five half-waves, as seen in Fig. 20(a)) of the profile ($P/P_{cr} = 1$) the behaviour is linear. For $P/P_{cr} > 1$, the curves evolve non-linearly but still increase with high slope due to well-known post-critical stiffness associated to the local buckling mode – the columns exhibit high post-buckling resistance, with an applied-to-critical load ratio (P/P_{cr}) higher than 2. Fig. 20(b)-(d) shows the column deformation shapes at the maximum load, together with the Hashin damage initiation index for matrix in compression and tension, and damage shear propagation index.

The difference in ultimate strength between the TM and NMs was found to be minimal, less than 3%. Furthermore, comparing both NMs with different maximum amplitudes ($0.13 \cdot t$ and $0.004 \cdot t$), no significant difference in ultimate strength was observed between them, but only minor differences in the post-buckling paths (as seen in the zoomed

detail in Fig. 19). At the ultimate load step, all three models exhibited a similar Hashin failure initiation criterion and damage propagation. Additionally, the failure mode was very similar for the three models, characterized by a local buckling mode shape with five half-waves. This mode shape was also identified by an elastic buckling analysis, illustrated in Fig. 20(a).

In resume, it can be concluded that modelling a pGFRP wide-section profile with nominal sizes and GI with the shape of the critical buckling mode and amplitude of $\sim 0.1 \cdot t$, effectively captures the essential nonlinear behaviour and strength of the column. This finding shows that the simple approach of modelling the imperfection by using the amplified critical buckling mode is accurate enough (at least for the studied case).

However, although the imperfections of member geometry were accounted for in this study, the imperfections of member material, such as the heterogeneity along the cross-section walls (flanges and web) and
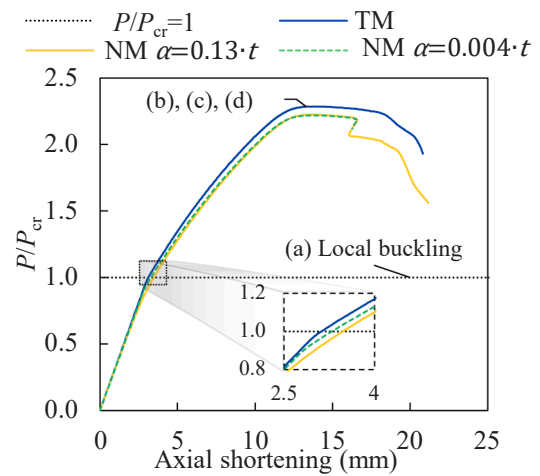
Fig. 19. Applied-to-critical load ratio (P/P_{cr}) vs. axial shortening of the pGFRP wide-section column (W152–6-2 specimen), for the "true" model (TM), and nominal models (NM) with maximum amplitudes of $0.13 \cdot t$ and $0.004 \cdot t$.
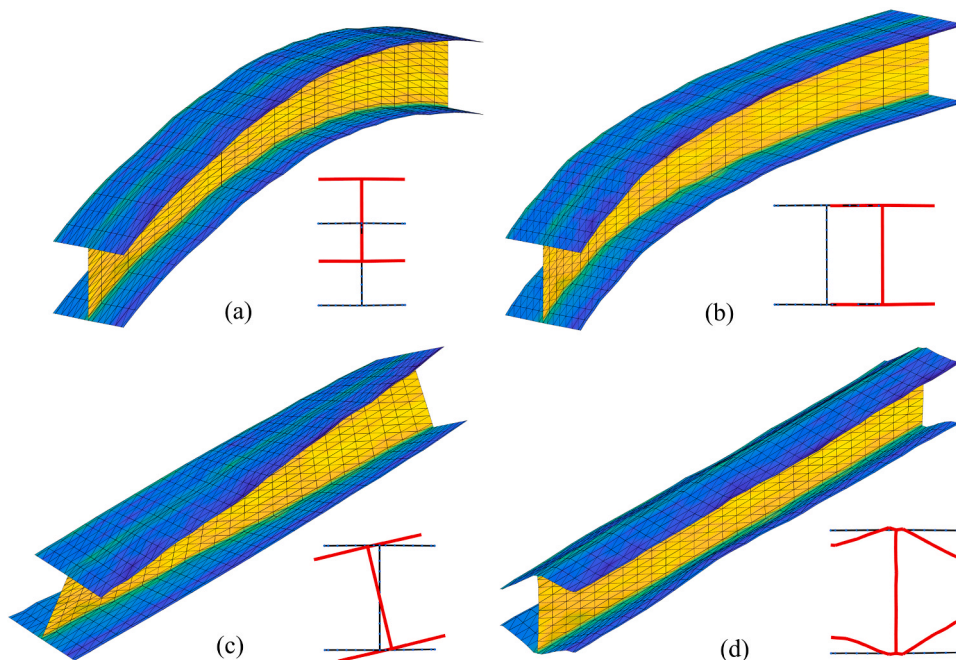
Fig. 18. GI modes amplified for the W152–6-2 specimen associated to (a) minor-axis GI, (b) major-axis GI, (c) twist GI and (d) local GI, with a thickness field colormap.
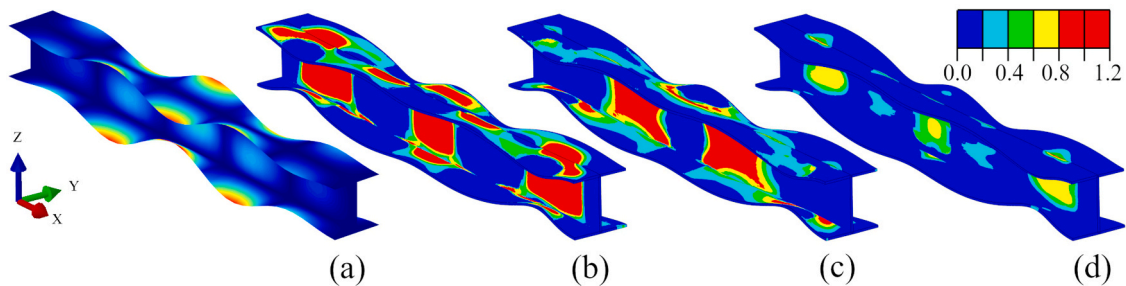
Fig. 20. Deformation shapes for: (a) the critical buckling shape, (b) the ultimate capacity with the matrix tensile initiation Hashin criterion colourmap, (c) matrix compressive initiation Hashin criterion colourmap, and (d) damage shear propagation for the as-measured model with thickness field.

web-flange junction, were not taken into account in the present computational model. Thus, further in-depth studies are required to better quantify the complex behaviour of overall cross-section under crushing, including the heterogeneity of different wall materials and several cross-section shapes. This subject is very relevant as it inevitably interacts with the buckling phenomena, potentially leading to a severe and abrupt reduction of the ultimate strength of the structural member.

7. Concluding remarks

This paper highlights the importance of and challenges in accurately determining the geometrical imperfections (GIs) of pultruded glass fibre reinforced polymer (pGFRP) profiles, and proposes a new modal approach to measure them. It also identifies the need for further research to widen the available database of GIs and improve the reliability of GI-based design formulas for the analysis and safety checking of pGFRP structures. In resume, the following concluding remarks are drawn:

1. The proposed methodology employs a highly accurate automatic 3D coordinate measuring machine (CMM) with a measurement accuracy of 0.010 mm to measure tri-dimensional coordinate points on both sides of prismatic pGFRP members.
2. The obtained point cloud data facilitates the determination of important size parameters, including height, width, thickness, and corner radius, along the longitudinal direction (length) and transversal direction (cross-section walls) of pGFRP members.
3. A point cloud transformation technique is introduced specifically for shell-type nodes, enhancing global mode decomposition (minor-axis, major-axis and twist GIs), and assessment of the local mode decomposition, considering the wall (plate-like) GIs.
4. The preliminary measurements presented herein (for a specific W-section) showed that flexural (major- and minor-axis) GIs exhibited a longitudinal shape very similar to a single half-wave. This confirms the assumption widely adopted in computational simulations of using the critical buckling mode, if it is of flexural nature. The twist GI showed a quasi-linear variation along the member length and the local GI exhibited a pattern (inward flange imperfection) almost constant along the member length.
5. The preliminary measurements of global and local GIs reported in this paper (for a specific W-section) led to moderately low amplitude values, compared to the manufacturing limits recommended by the existing standards [30,46,55].
6. The inclusion of measured GIs in finite element (FE) models offers a more realistic representation compared to the conventional practice of using the critical buckling mode as a GI shape.
7. The FE model with incorporation of measured GIs of a wide-flange pGFRP column led to a strength estimate close to the one using the nominal dimensions provided by the manufacturer, along with a GI with the shape of the critical (local) buckling mode and the maximum measured amplitude. Both models differed only in the GI shape, which affected the results only by 3%.

This paper presented a general approach to characterize GIs of pGFRP profiles and its procedures and operations; however, this methodology was applied only to a few members and cross-section shapes, so no general conclusions about GIs of pGFRP profiles can be drawn at this stage. Future work will focus on the application of this approach to acquire wide relevant GI information of pGFRP members with various cross-section shapes (I, H, L, U, and Box). Statistical treatment will be conducted to better quantify probability functions that accurately represent the random behaviour of GIs and DDs. In summary, the current work has two important future goals: (i) to enable an increased accuracy of computational simulations of imperfect pGFRP members, and (ii) to improve the calibration and reliability of strength curves for the design of pGFRP members. These advances on the knowledge of GIs will enhance the overall performance of pGFRP members, ensuring compliance with international standards and promoting the quality control and safety of pGFRP structures.

CRediT authorship contribution statement

Correia João: Writing – review & editing, Resources, Methodology, Conceptualization. **Silvestre Nuno:** Writing – review & editing, Supervision, Resources, Project administration, Methodology, Funding acquisition, Conceptualization. **Ribeiro Álvaro:** Writing – review & editing, Resources. **Pinheiro Alexandre:** Validation, Software, Methodology, Investigation, Data curation. **Lazzari João:** Writing – original draft, Visualization, Validation, Software, Methodology, Formal analysis, Data curation, Conceptualization. **Martins Luís:** Writing – review & editing, Resources, Methodology, Data curation, Conceptualization.

Declaration of generative AI and AI-assisted technologies in the writing process

During the preparation of this work the first author used OpenAI's tool ChatGPT in order to enhance the language and readability of the first draft. After using this tool/service, the authors reviewed and edited the content as needed and take full responsibility for the content of the publication.

Declaration of Competing Interest

The authors declare that they have no known competing financial interests or personal relationships that could have appeared to influence the work reported in this paper.

Data Availability

Data will be made available on request.

Acknowledgments

References

[1] J.R. Correia, Pultrusion of advanced composites, in: J. Bai (Ed.), Advanced Fiber-Reinforced Polymer(FRP) Composites for Structural Applications, Second, Woodhead Publishing, Elsevier, 2023, pp. 137–177, https://doi.org/10.1016/B978-0-12-820346-0.00007-1.

[2] L.C. Bank, Composites for Construction: Structural Design with FRP Materials, Wiley, New Jersey, 2006, https://doi.org/10.1002/9780470121429.

[3] S. Russo, A review on buckling collapses of simple and complex columns made from pultruded FRP material, Compos.: Mech., Comput., Appl.: Int. J. 8 (2017) 1–34, https://doi.org/10.1615/CompMechComputApplIntJ.v8.i1.10.

[4] K.J.R. Rasmussen, G.J. Hancock, Geometric imperfections in plated structures subject to interaction between buckling modes, Thin-Walled Struct. 6 (1988) 433–452, https://doi.org/10.1016/0263-8231(88)90012-2.

[5] B. Young, K.J.R. Rasmussen, Compression Tests of Fixed-Ended and Pin-Ended Cold-Formed Lipped Channels, Research Report - University of Sydney, School of Civil and Mining Engineering. (1995).

[6] B.W. Schafer, T. Peköz, Computational modeling of cold-formed steel: characterizing geometric imperfections and residual stresses, J. Constr. Steel Res 47 (1998) 193–210, https://doi.org/10.1016/S0143-974X(98)00007-8.

[7] V. Zeinoddini-Meimand, Geometric Imperfections in Cold-Formed Steel Members, PhD Thesis, Johns Hopkins University, Baltimore, Maryland, 2011.

[8] V.M. Zeinoddini, B.W. Schafer, Simulation of geometric imperfections in cold-formed steel members using spectral representation approach, Thin-Walled Struct. 60 (2012) 105–117, https://doi.org/10.1016/j.tws.2012.07.001.

[9] E.S. Santos, E.M. Batista, D. Camotim, Experimental investigation concerning lipped channel columns undergoing local–distortional–global buckling mode interaction, Thin-Walled Struct. 54 (2012) 19–34, https://doi.org/10.1016/j.tws.2012.02.004.

[10] G.Y. Matsubara, E. de M. Batista, G.C. Salles, Lipped channel cold-formed steel columns under local-distortional buckling mode interaction, Thin-Walled Struct. 137 (2019) 251–270, https://doi.org/10.1016/j.tws.2018.12.041.

[11] W.S. Santos, A. Landesmann, D. Camotim, Distortional strength of end-bolted CFS lipped channel columns: experimental investigation, numerical simulations and DSM design, Thin-Walled Struct. 148 (2020) 106469, https://doi.org/10.1016/j.tws.2019.106469.

[12] X. Zhao, M. Tootkaboni, B.W. Schafer, Laser-based cross-section measurement of cold-formed steel members: model reconstruction and application, Thin-Walled Struct. 120 (2017) 70–80, https://doi.org/10.1016/J.TWS.2017.08.016.

[13] S. Selvaraj, M. Madhavan, Geometric imperfection measurements and validations on cold-formed steel channels using 3D noncontact laser scanner, J. Struct. Eng. 144 (2018) 04018010, https://doi.org/10.1061/(ASCE)ST.1943-541X.0001993.

[14] P. Feng, Y. Zou, L. Hu, T.Q. Liu, Use of 3D laser scanning on evaluating reduction of initial geometric imperfection of steel column with pre-stressed CFRP, Eng. Struct. 198 (2019) 109527, https://doi.org/10.1016/J.ENGSTRUCT.2019.109527.

[15] L. Gardner, P. Kyvelou, G. Herbert, C. Buchanan, Testing and initial verification of the world's first metal 3D printed bridge, J. Constr. Steel Res 172 (2020) 106233, https://doi.org/10.1016/J.JCSR.2020.106233.

[16] Z. Zhang, G. Shi, L. Hou, L. Zhou, Geometric dimension and imperfection measurements of box-T section columns using 3D scanning, J. Constr. Steel Res 183 (2021) 106742, https://doi.org/10.1016/J.JCSR.2021.106742.

[17] B. Güldür Erkal, Ö.G. Çağrıcı, Automated geometric imperfection detection and quantification of CFS members from point clouds, KSCE J. Civ. Eng. 26 (2022) 3888–3904, https://doi.org/10.1007/s12205-022-0795-9.

[18] S. Nascimento, J.J. Oliveira Pedro, R. Santos, U. Kuhlmann, Experimental behaviour of plate girders in steel – internal forces in intermediate transverse stiffeners, Eng. Struct. 291 (2023) 116425, https://doi.org/10.1016/j.engstruct.2023.116425.

[19] Y. Xu, B. Wu, B. Zheng, Full-field geometric imperfection and effect on cross-section capacity of circular steel tubes, J. Constr. Steel Res 201 (2023) 107749, https://doi.org/10.1016/J.JCSR.2022.107749.

[20] D. Xu, Y. Wang, X. Liu, B. Chen, Y. Bu, A novel method and modelling technique for determining the initial geometric imperfection of steel members using 3D scanning, Structures 49 (2023) 855–874, https://doi.org/10.1016/J.ISTRUC.2023.01.136.

[21] S. Farzanian, A. Louhghalam, B.W. Schafer, M. Tootkaboni, Geometric imperfections in CFS structural members: part i: a review of the basics and some modeling strategies, Thin-Walled Struct. 186 (2023) 110619, https://doi.org/10.1016/j.tws.2023.110619.

[22] H.S. Park, H.M. Lee, H. Adeli, I. Lee, A new approach for health monitoring of structures: terrestrial laser scanning, Comput. -Aided Civ. Infrastruct. Eng. 22 (2007) 19–30, https://doi.org/10.1111/J.1467-8667.2006.00466.X.

[23] G.C. Salles, E. de, M. Batista, D.C.T. Cardoso, A modal decomposition approach for experimental buckling analysis of thin-walled lipped channel columns, Eng. Struct. 256 (2022) 113979, https://doi.org/10.1016/j.engstruct.2022.113979.

[24] G.C. Salles, E. de, M. Batista, D.C.T. Cardoso, Extension of modal decomposition approach for buckling analysis of thin-walled lipped channel columns: local,

[25] distortional, flexural and torsional modes, Thin-Walled Struct. 181 (2022) 110127, https://doi.org/10.1016/j.tws.2022.110127.

[25] American Iron and Steel Institute, AISI S240–15 North American Standard for Cold-Formed Steel Structural Framing, ANSI, 2015.

[26] Australian/New Zealand Standard, AS/NZS 4600 - Cold-Formed Steel Structures, 3rd ed., Sydney, Australia, 2018.

[27] Associação Brasileira de Normas Técnicas, NBR 14762 - Design of Cold-Formed Steel Structures (in Portuguese), Rio de Janeiro, Brazil, 2010.

[28] European Committee for Standardization, EN 1993–1-3 - Eurocode 3: Design of Steel Structures - Part 1–3: General Rules - Supplementary Rules for Cold-Formed Members and Sheeting, Brussels, 2006.

[29] Soon Jong Yoon, Local Buckling of Pultruded I-Shape Columns, PhDThesis, Georgia Institute of Technology, Atlanta, Georgia, 1993.

[30] American Society for Testing and Materials, ASTM D3917 − 15a - Standard Specification for Dimensional Tolerance of Thermosetting Glass-Reinforced Plastic Pultruded Shapes 1, 2015. https://doi.org/10.1520/D3917–15A.

[31] R.J. Brooks, G.J. Turvey, Lateral buckling of pultruded GRP I-section cantilevers, Compos Struct. 32 (1995) 203–215, https://doi.org/10.1016/0263-8223(95)00018-6.

[32] A. Zureick, D. Scott, Short-term behavior and design of fiber-reinforced polymeric slender members under axial compression, J. Compos. Constr. 1 (1997) 140–149, https://doi.org/10.1061/(asce)1090-0268(1997)1:4(140).

[33] A. Zureick, R. Steffen, Behavior and design of concentrically loaded pultruded angle struts, J. Struct. Eng. 126 (2000) 406–416.

[34] A. Lane, J.T. Mottram, Influence of modal coupling on the buckling of concentrically loaded pultruded fibre-reinforced plastic columns, in: Proc Instn Mech Engrs Vol 216 Part L, J. Mater.: Des. Appl. (2002) 133–144, https://doi.org/10.1243/146442002320139333.

[35] J.T. Mottram, N.D. Brown, D. Anderson, Physical testing for concentrically loaded columns of pultruded glass fibre reinforced plastic profile, Proc. Inst. Civ. Eng. - Struct. Build. 156 (2003) 205–219, https://doi.org/10.1680/stbu.2003.156.2.205.

[36] T.T. Nguyen, T.M. Chan, J.T. Mottram, Lateral-torsional buckling resistance by testing for pultruded FRP beams under different loading and displacement boundary conditions, Compos B Eng. 60 (2014) 306–318, https://doi.org/10.1016/j.compositesb.2013.12.025.

[37] T.T. Nguyen, Lateral-Torsional Buckling Resistance of Pultruded Fibre Reinforced Polymer Shapes, PhD Thesis, University of Warwick, Coventry, 2014. http://webcat.warwick.ac.uk/record=b2746131~S1 (accessed March 19, 2023).

[38] D. Cardoso, K.A. Harries, E.M. Batista, Compressive strength equation for GFRP square tube columns, Compos B Eng. 59 (2014) 1–11, https://doi.org/10.1016/j.compositesb.2013.10.057.

[39] E.V. Southwell, On the analysis of experimental observations in problems of elastic stability, Proc. R. Soc. Lond. 135 (1932) 601–616.

[40] A. Monteiro, Theoretical and Experimental Analysis of Pultruded GFRP Angles Under Compression, Master Dissertation in Civil Engineering (in Portuguese), School of Engineering of São Carlos, University of São Paulo, São Carlos, SP, Brazil, 2020. http://sistemas.set.eesc.usp.br/producao/1230 (accessed July 4, 2022).

[41] G.J. Turvey, Y. Zhang, A computational and experimental analysis of the buckling, postbuckling and initial failure of pultruded GRP columns, Comput. Struct. 84 (2006) 1527–1537, https://doi.org/10.1016/j.compstruc.2006.01.028.

[42] F. Laudiero, F. Minghini, N. Tullini, Postbuckling failure analysis of pultruded FRP beams under uniform bending, Compos B Eng. 54 (2013) 431–438, https://doi.org/10.1016/j.compositesb.2013.06.009.

[43] F. Laudiero, F. Minghini, N. Tullini, Buckling and postbuckling finite-element analysis of pultruded FRP profiles under pure compression, 04013026, J. Compos. Constr. 18 (2013), https://doi.org/10.1061/(ASCE)CC.1943-5614.0000384.

[44] Creative Pultrusions, The New and Improved Pultex Pultrusion Design Manual of Standard and Custom Fiber Reinforced Polymer Structural Profiles, Vol. 4, Rev. 6, Alum Bank: Creative Pultrusions, Inc, 2004.

[45] Strongwell, EXTREN® Design Manual (Bristol), Strongwell Corp., Bristol, 2010.

[46] European Standard, EN 13706–2:2002 - Reinforced Plastics Composites — Specifications for Pultruded Profiles — Part 2: Method of Test and General Requirements, 3 (2002).

[47] L. Ascione, V.P. Berardi, A. Giordano, S. Spadea, Pre-buckling imperfection sensitivity of pultruded FRP profiles, Compos B Eng. 72 (2015) 206–212, https://doi.org/10.1016/J.COMPOSITESB.2014.12.014.

[48] F. Nunes, J.R. Correia, N. Silvestre, Structural behavior of hybrid FRP pultruded beams: experimental, numerical and analytical studies, Thin-Walled Struct. 106 (2016) 201–217, https://doi.org/10.1016/j.tws.2016.05.004.

[49] F. Nunes, N. Silvestre, J.R. Correia, Structural behaviour of hybrid FRP pultruded columns. Part 2: numerical study, Compos Struct. 139 (2016) 304–319, https://doi.org/10.1016/j.compstruct.2015.12.059.

[50] H. Chawla, S.B. Singh, Stability and failure characterization of fiber reinforced pultruded beams with different stiffening elements, part 2: analytical and numerical studies, Thin-Walled Struct. 141 (2019) 606–626, https://doi.org/10.1016/J.TWS.2018.10.024.

[51] T.T. Nguyen, S. Selvaraj, T.M. Chan, J.T. Mottram, Influence of combined imperfections on lateral-torsional buckling behaviour of pultruded FRP beams, Compos Struct. 304 (2023) 116385, https://doi.org/10.1016/J.COMPSTRUCT.2022.116385.

[52] M. Anbarasu, M. Kasiviswanathan, M. Kathiresan, G. Mohan Ganesh, Numerical parametric study and design of pultruded GFRP composite channel columns, Vol. 15, Page 837, Sustainability 2023 15 (2023) 837, https://doi.org/10.3390/SU15010837.

[53] P. Czapski, T. Kubiak, Numerical and experimental investigations of the post-buckling behaviour of square cross-section composite tubes, Compos Struct. 132 (2015) 1160–1167, https://doi.org/10.1016/J.COMPSTRUCT.2015.07.039.

[54] Fiberline, Fiberline Design Manual - Chapter 8: Fiberline Standard Tolerances, Fiberline Composites A/S, Kolding, Denmark, 2002. https://fiberline.com/design-manual (accessed March 22, 2023).

[55] National Standard of the People's Republic of China, GB/T 31539–2015E - Pultruded Fibre Reinforced Polymer Composites Structural Profiles (English Translation), China Building Materials Federation. (2015).

[56] F. Nunes, N. Silvestre, J.R. Correia, Structural behaviour of hybrid FRP pultruded columns. Part 2: numerical study, Compos Struct. 139 (2016) 304–319, https://doi.org/10.1016/j.compstruct.2015.12.059.

[57] N.M.F. Silva, D. Camotim, N. Silvestre, J.R. Correia, F.A. Branco, First-order, buckling and post-buckling behaviour of GFRP pultruded beams. Part 2: numerical simulation, Comput. Struct. 89 (2011) 2065–2078, https://doi.org/10.1016/j.compstruc.2011.07.006.

[58] T. Kubiak, Z. Kolakowski, J. Swiniarski, M. Urbaniak, A. Gliszczynski, Local buckling and post-buckling of composite channel-section beams - numerical and experimental investigations, Compos B Eng. 91 (2016) 176–188, https://doi.org/10.1016/j.compositesb.2016.01.053.

[59] National Research Council of Italy NRCI, CNR-DT 205/2007 - Advisory Committee on Technical Recommendations for Construction - Guide for the Design and Construction of Structures made of FRP Pultruded Elements, Rome, Italy, 2008.

[60] American Composites Manufacturers Association, Pre-Standard for Load and Resistance Factor Design (LRFD) of Pultruded Fiber Reinforced Polymer (FRP) Structures (Final), Structural Engineers Institute SEI-ASCE, Reston, VA, 2010.

[61] CROW-CUR, Recommendation 96:2019 - Fibre Reinforced Polymers in Buildings & Civil Engineering Structures – Recommendation 96:2019, Gouda, The Netherlands, 2019.

[62] Standard of China Engineering Construction Standardization Association, T/CECS 692–2020 - Technical Specification for Structure of Pultruded Fiber Reinforced Polymer Composites (in Chinese), China Construction Industry, Beijing, China, 2020.

[63] European Committee for Standardization, CEN/TS 19101:2022 - Design of Fibre-Polymer Composite Structures, Technical Committee CEN/TC 250, Brussels, Belgium, 2022.

[64] International Organization for Standardization, ISO 10360–1:2000 - Geometrical Product Specifications (GPS) — Acceptance and Reverification Tests for Coordinate Measuring Machines (CMM) — Part 1: Vocabulary, Switzerland, 2000. https://www.iso.org/standard/18418.html (accessed March 21, 2023).

[65] D. Flack, Good Practice Guide No. 41 CMM Measurement Strategies Issue 2, Hampton Road, Teddington, Middlesex, 2014. https://www.npl.co.uk/gpgs/cmm-measurement-strategies (accessed April 18, 2023).

[66] British Standard Institution, BS 7172:1989, British Standard Guide to Assessment of Position, Size and Departure from Nominal Form Geometric Features, BSI, London. (1989) 1–17.

[67] V. Pratt, Direct least-squares fitting of algebraic surfaces, ACM SIGGRAPH Comput. Graph. 21 (1987) 145–152, https://doi.org/10.1145/37402.37420.

[68] The MathWorks Inc., MATLAB Version: 9.13.0.2126072 (R2022b) Update 3, (2022). https://www.mathworks.com.

[69] L. Euler, Nova methodus motum corporum rigidorum degerminandi, Euler Archive - All Works. 479 (1776). https://scholarlycommons.pacific.edu/euler-works/479.

[70] O. Rodrigues, Des lois géométriques qui régissent les déplacements d'un système solide dans l'espace, et de la variation des coordonnées provenant de ces déplacements considérés indépendamment des causes qui peuvent les produire, J Math Pures Appl, 1e série 5 (1840). http://www.numdam.org/item/JMPA_1840_1_5_380_0/.

[71] Strongwell, EXTREN® Fiberglass Structural Shapes and Plate, (2020). https://www.strongwell.com/products/structural-shapes-and-plate/ (accessed July 23, 2022).

[72] Dassault Systèmes Simulia Corp., Abaqus/CAE 2018, (2018).

[73] A.M. Girão Coelho, J. Toby Mottram, K.A. Harries, Finite element guidelines for simulation of fibre-tension dominated failures in composite materials validated by case studies, Compos Struct. 126 (2015) 299–313, https://doi.org/10.1016/J.COMPSTRUCT.2015.02.071.

[74] L. Almeida-Fernandes, N. Silvestre, J.R. Correia, M.R.T. Arruda, Fracture toughness-based models for damage simulation of pultruded GFRP materials, Compos B Eng. 186 (2020), https://doi.org/10.1016/j.compositesb.2020.107818.

[75] L. Almeida-Fernandes, J.R. Correia, N. Silvestre, Transverse fracture behavior of pultruded GFRP materials in tension: effect of fiber layup, 04020019, J. Compos. Constr. 24 (2020), https://doi.org/10.1061/(asce)cc.1943-5614.0001024.

[76] E. Riks, An incremental approach to the solution of snapping and buckling problems, Int J Solids Struct. 15 (1979) 529–551, https://doi.org/10.1016/0020-7683(79)90081-7.

[77] Z. Hashin, A. Rotem, A Fatigue failure criterion for fiber reinforced materials, J. Compos Mater. 7 (1973) 448–464, https://doi.org/10.1177/002199837300700404.

[78] Z. Hashin, Failure criteria for unidirectional fiber composites, J. Appl. Mech. 47 (1980) 329–334.

[79] A.P.C. Duarte, A. Díaz Sáez, N. Silvestre, Comparative study between XFEM and Hashin damage criterion applied to failure of composites, Thin-Walled Struct. 115 (2017) 277–288, https://doi.org/10.1016/j.tws.2017.02.020.

[80] B. Lopes, M.R.T. Arruda, L. Almeida-Fernandes, L. Castro, N. Silvestre, J.R. Correia, Assessment of mesh dependency in the numerical simulation of compact tension tests for orthotropic materials, Compos. Part C: Open Access 1 (2020) 100006, https://doi.org/10.1016/j.jcomc.2020.100006.

[81] S. Ádány, B.W. Schafer, A full modal decomposition of thin-walled, single-branched open cross-section members via the constrained finite strip method, J. Constr. Steel Res 64 (2008) 12–29, https://doi.org/10.1016/J.JCSR.2007.04.004.

[82] P.B. Dinis, D. Camotim, N. Silvestre, GBT formulation to analyse the buckling behaviour of thin-walled members with arbitrarily "branched" open cross-sections, Thin-Walled Struct. 44 (2006) 20–38, https://doi.org/10.1016/J.TWS.2005.09.005.